Terrestrial Gamma-ray Flashes in the Fermi Era: Improved Observations and Analysis Methods

Michael S. Briggs,[1,2] Shaolin Xiong,[1] Valerie Connaughton,[1,2]

Dave Tierney,[3] Gerard Fitzpatrick,[3] Suzanne Foley,[3] J. Eric Grove,[4]

Alexandre Chekhtman,[5] Melissa Gibby,[6] Gerald J. Fishman,[6,7]

Shelia McBreen,[3] Vandiver L. Chaplin,[1] Sylvain Guiriec,[8,9] Emily Layden,[1]

P. N. Bhat,[1] Maximilian Hughes,[10] Jochen Greiner,[11] Andreas von Kienlin,[11]

R. Marc Kippen,[12] Charles A. Meegan,[13] William S. Paciesas,[13]

Robert D. Preece,[1,2] Colleen Wilson-Hodge,[14] Robert H. Holzworth[15] and

Michael L. Hutchins[15]

Accepted for publication in the Journal of Geophysical Research − Space Physics.

P. N. Bhat, M. S. Briggs, V. L. Chaplin, V. Connaughton, E. Layden, R. D. Preece and S. Xiong, CSPAR, 320 Sparkman Drive, Huntsville, AL, 35805, USA. (michael.briggs@uah.edu).

G. Fitzpatrick, Suzanne Foley, S. McBreen and D. Tierney, School of Physics, University College Dublin, Belfield, Dublin 4, Ireland. (sheila.mcbreen@ucd.ie)

A. Chekhtman and J. Eric Grove, Space Science Division, U. S. Naval Research Laboratory, Washington, D.C., 20375, USA. (eric.grove@nrl.navy.mil)

G. J. Fishman and M. Gibby, Jacobs Engineering Group Inc., 1500 Perimeter Parkway, Huntsville, AL 35806, USA. (jerry.fishman@nasa.gov)

C. Wilson-Hodge, Space Science Office, VP62, NASA Marshall Space Flight Center, Huntsville, AL, 35812, USA. (Colleen.Wilson@nasa.gov)

S. Guiriec, NASA Goddard Space Flight Center, Greenbelt, MD 20771, USA. (sylvain.guiriec@nasa.gov)

R. M. Kippen, ISR-1, Los Alamos National Laboratory, Los Alamos, NM 87545, USA. (mkippen@lanl.gov)

C. A. Meegan and W. S. Paciesas, USRA, 320 Sparkman Drive, Huntsville, AL, 35805, USA. (chip.meegan@nasa.gov).

Maximilian Hughes, Department of Physics & Astronomy, Clemson University, Clemson, SC 29631, USA. (maximih@g.clemson.edu)

J. Greiner and A. von Kienlin, Max-Planck Institut für extraterrestrische Physik, D-85741 Garching, Germany. (azk@mpe.mpg.de)

Abstract. A new data mode and new analysis methods are used to detect Terrestrial Gamma-ray Flashes (TGFs) with the Fermi Gamma-ray Burst Monitor (GBM) ten times more frequently than previously. In 1037 hours of observations at times and over regions for

R. H. Holzworth and M. L. Hutchins, Earth and Space Sciences, University of Washington, Seattle, WA 98195, USA. (bobholz@ess.washington.edu)

[1]CSPAR, University of Alabama in Huntsville, Huntsville, AL, 35899, USA

[2]Dept. of Physics, University of Alabama in Huntsville, Huntsville, AL, 35899, USA

[3]University College Dublin, Belfield, Dublin 4, Ireland

[4]Space Science Division, U. S. Naval Research Laboratory, Washington, D.C., 20375, USA

[5]George Mason University, Fairfax, VA, 22030, USA

[6]Jacobs Engineering Group Inc., Huntsville, AL 35806, USA.

[7]previous: Space Science Office, NASA Marshall Space Flight Center, Huntsville, AL, 35812, USA

which TGFs are expected, 384 new TGFs were found in addition to the 39 TGFs and two Terrestrial Electron Beam events already detected

[8]NASA Postdoctoral Program Fellow, Goddard Space Flight Center, Greenbelt, MD 20771, USA

[9]previous: CSPAR, University of Alabama in Huntsville, Huntsville, AL, 35899, USA

[10]Department of Physics & Astronomy, Clemson University, Clemson, SC 29631, USA

[11]Max-Planck Institut für extraterrestrische Physik, D-85741 Garching, Germany

[12]ISR-1, Los Alamos National Laboratory, Los Alamos, NM 87545, USA

[13]Universities Space Research Association, Huntsville, AL, 35803, USA

[14]Space Science Office, NASA Marshall Space Flight Center, Huntsville, AL, 35812, USA

[15]Earth and Space Sciences, University of Washington, Seattle, WA 98195, USA

without the new data mode and methodology. Cosmic ray showers were found to be an important background; they show characteristic signatures in the data of both GBM and the Fermi Large Area Telescope Calorimeter that enable their removal, leaving a sample estimated to consist of ≈98% TGFs. The sample includes shorter TGFs than previously found with GBM. The true duration distribution likely contains additional short TGFs because their detection by GBM is limited by detector deadtime. One-third of this sample has matches with locations from the World Wide Lightning Location Network (WWLLN) –maps of these locations show the geographic and meteorological features more clearly than maps of spacecraft locations. The intrinsic TGF rate is evaluated using the lightning rate maps of the Lightning Imaging Sensor, accounting for the detection efficiency of GBM as a function of spacecraft-source offset, from which we estimate a global TGF rate of ≈400,000 per year. With continuous production of data in the new mode we estimate that GBM will detect ≈850 TGFs per year.

1. Introduction

1.1. Terrestrial Gamma-ray Flashes

In the past several decades thunderstorms and lightning have been observed to emit high-energy radiation in a range of phenomena – *Dwyer et al.* [2012a] provide a comprehensive review of the emerging field of high-energy atmospheric physics. The most remarkable of these phenomena, easily detectable from hundreds of km above the Earth as extremely intense sub-millisecond pulses of gamma rays, are Terrestrial Gamma-ray Flashes (TGFs). The microphysics is understood as the acceleration of electrons by the Relativistic Runaway Electron Avalanche (RREA) process, followed by the emission of gamma rays via bremsstrahlung [*Gurevich et al.*, 1992]. Relativistic feedback is an additional process by which Compton backscattering and pair-production of the bremsstrahlung photons produce additional seed electrons and therefore not just avalanche multiplication but additionally the multiplication of avalanches. Relativistic feedback may be the process that distinguishes TGFs from other high-energy photon emission by thunderstorms, causing the extreme intensities and short timescale of TGFs [*Dwyer*, 2003, 2008]. Alternatively *Carlson et al.* [2010] and *Celestin and Pasko* [2011] suggest that runaway electrons are produced and accelerated in the strong fields of lightning leaders. TGFs are also observed as Terrestrial Electron Beams (TEBs): propagating through the atmosphere, the gamma rays of a TGF produce secondary electrons and positrons by Compton scattering and pair production. At altitudes where scattering is improbable, these charged particles follow the magnetic field line and are therefore confined in a beam. While the magnetic beaming makes it possible to detect TEBs at great distances from the sources it makes detections less frequent since the

beam cross section is smaller than that of the unconfined parent photons [*Dwyer et al.*, 2008; *Carlson et al.*, 2011; *Briggs et al.*, 2011].

TGFs were discovered from space with the Burst and Transient Source Experiment (BATSE) on the Compton Gamma Ray Observatory [*Fishman et al.*, 1994] and since then have mostly been observed with space-based instruments, including the Reuven Ramaty High Energy Solar Spectroscopic Imager (RHESSI) [*Smith et al.*, 2005; *Grefenstette et al.*, 2009], the Astrorivelatore Gamma a Immagini Leggero (AGILE) [*Marisaldi et al.*, 2010a, b; *Fuschino et al.*, 2011; *Tavani et al.*, 2011], and the Gamma-ray Burst Monitor (GBM) on the Fermi Gamma-ray Space Telescope [*Briggs et al.*, 2010; *Connaughton et al.*, 2010; *Briggs et al.*, 2011; *Fishman et al.*, 2011]. Two TGFs have been observed from the ground, one initiated by rocket-triggered lightning [*Dwyer et al.*, 2004] and another from natural lightning [*Dwyer et al.*, 2012b]; one TGF has been observed from an aircraft, with the Airborne Detector for Energetic Lightning Emissions (ADELE) instrument [*Smith et al.*, 2011a].

1.2. TGF Detection

Several techniques have been used to detect TGFs and TEBs. BATSE used on-board software to monitor the detector rates on timescales of 64 ms and longer, activating a "trigger" mode when higher rates were detected to collect data with higher temporal resolution [*Fishman et al.*, 1994]. The 64 ms hardware-based sampling intervals are much longer than TGFs and therefore include additional background counts without gaining additional TGF signal, thereby reducing the signal-to-noise ratio and the sensitivity of BATSE to TGFs [*Grefenstette et al.*, 2008]. In contrast, data of individual counts are transmitted to the ground by RHESSI, enabling an offline search at high temporal

resolution [*Grefenstette et al.*, 2009; *Gjesteland et al.*, 2012]. (The term "count" is used because a particular measurement in a detector might be from a gamma ray, possibly from a TGF, or from a charged particle, from a TEB or a cosmic ray or a radioactive decay.) AGILE uses a combination method, with on-board triggering followed by offline examination to filter out a substantial number of noise triggers [*Marisaldi et al.*, 2010a].

1.3. The Fermi Gamma-ray Space Telescope

The Fermi Gamma-ray Space Telescope observes the high-energy universe in gamma rays. Primarily intended for astrophysical observations of objects such as gamma-ray bursts (GRBs), active galactic-nuclei, pulsars, supernova remnants, diffuse emission, cosmic rays and dark matter, Fermi also observes gamma rays from the solar system, from the Sun, Earth and Moon due to cosmic ray interactions, from the Sun from solar flares, and from the Earth from TGFs. Fermi consists of two instruments, the Large Area Telescope (LAT) and GBM. Fermi has a nearly circular orbit of 565 km altitude with an orbital inclination of 25.6° that causes it primarily to overfly the tropics, where thunderstorms and TGFs are common.

The LAT is a pair-conversion telescope designed to detect gamma rays from ≈ 20 MeV to more than 300 GeV [*Atwood et al.*, 2009]. The LAT consists of three detector systems – tracker, calorimeter, and anti-coincidence detector – to image and measure the energy of gamma rays over this wide energy range and discriminate between gamma rays and the charged-particle background. The tracker is an array of silicon strip detectors (SSDs) alternating with tungsten foils intended to convert a gamma ray into a positron-electron pair, which is tracked in the SSDs to determine the incident direction. Typically the pair propagates into the calorimeter, a hodoscopic array of cesium iodide

(CsI(Tl)) scintillating crystal bars that measure the energy of an incident gamma ray from the properties of the developing electromagnetic shower. The anti-coincidence detector is an array of plastic scintillator tiles that surrounds the tracker and calorimeter on the top and sides to tag most charged particles. The strong background rejection that is required for LAT's primary gamma-ray astrophysics science mission is enabled by the high segmentation of all three detector systems, with their ability to image the interactions of gamma rays and particle backgrounds in fine detail.

GBM extends the energy range of Fermi, observing from ≈8 keV to ≈40 MeV with two types of scintillation detectors [*Meegan et al.*, 2009]. The twelve sodium iodide (NaI) scintillation detectors observe from ≈8 keV to 1 MeV, while the two bismuth germanate (BGO) scintillation detectors cover the range from ≈ 200 keV to 40 MeV. For normally incident photons, the effective area of a NaI detector exceeds 100 cm^2 from 20 to 200 keV, but the effective area falls rapidly at higher energies due to the thinness of the detectors. The effective area of a GBM BGO detector ranges from 160 cm^2 to 200 cm^2, depending on the energy and direction of the photon. The fourteen detectors of GBM are arranged to view the entire sky not blocked by the Earth, with half of the detectors on one side of the spacecraft and the other half on the opposite side. The spectra of TGFs include gamma rays of sufficiently high energy that GBM readily observes TGFs even outside of its nominal field of view.

1.4. GBM on-board TGF detection

Similar to BATSE, GBM was also designed to use the triggering method to detect short transients such as gamma-ray bursts, soft-gamma repeaters, solar flares and TGFs. Data from the detectors are monitored by the flight software for statistically significant

rate increases. The hardware design limits the data available to the flight computer for this purpose to data binned at temporal resolutions of 16 ms and longer. Originally the GBM triggering software monitored only the rates of the twelve sodium iodide (NaI) detectors. The triggering algorithm was improved to also use the data of the two BGO detectors on 10 November 2009, 487 days after triggering was first enabled [*Fishman et al.*, 2011]. With their higher energy range and large effective area for gamma rays, the BGO detectors obtain a better signal from TGFs and TEBs. The use of the BGO detectors for triggering improved the average GBM TGF detection rate from one per 32.5 days to one per 4.0 days.

The on-board triggering of GBM still has reduced sensitivity compared to the capabilities of the detectors because the 16 ms minimum resolution of the data used for triggering is much longer than the duration of most TGFs. The reduction in sensitivity is similar to that of BATSE, but not as severe due to the shorter accumulation interval and lower deadtime of GBM [*Grefenstette et al.*, 2008; *Briggs et al.*, 2011; *Fishman et al.*, 2011].

1.5. Purposes

In this paper we report a new method for detecting GBM TGFs in which individual count data are downlinked for selected portions of the orbit and searched offline at sub-ms temporal resolution, improving the detection sensitivity of GBM for TGFs. Numerous additional TGFs are detected, creating a new large TGF sample. The reliability of the sample is demonstrated with several tests. We report the characteristics of this new TGF sample. The new sample includes TGFs with shorter durations than the triggered sample and the distribution of spacecraft nadir-to-source offsets extends to

larger distances. The sub-sample with accurate locations from associated VLF radio observations more clearly shows the geographic and meteorological patterns of the sources. We use this sample to estimate the TGF-lightning ratio and the global rate of TGFs.

2. Enhanced Data, TGF Search and Sample

2.1. Enhanced TTE Data Collection

GBM has a Time-Tagged Event (TTE) datatype in which the energies and arrival times of individual counts are recorded with 2 μs temporal resolution, several μs absolute accuracy, and energy resolution of 128 pseudo-logarithmic channels. Approximately 330 s of TTE data are generated in response to a trigger, consisting of $\approx$30 s of data before and 300 s after the rate increase that caused the trigger. Producing this datatype continuously would exceed the original telemetry allocation of GBM. Beginning 9 July 2010 increased telemetry was provided to support TTE production for a portion of each day. To use this resource most effectively, continuous (i.e., non-trigger) TTE data are produced in regions where high TGF activity is expected. Polygonal geographic regions were defined: TTE is commanded on when Fermi enters one of these regions and commanded off when Fermi exits. The GBM flight software was improved to support this new operational mode. Figure 1 shows the first region, for the Americas, used from 9 July 2010 to 3 November 2010. When the Northern Hemisphere summer thunderstorm season ended, Africa and Australia regions were implemented. On 27 Jan 2011 these two regions were increased in area. Additional changes were made as the seasons progressed (Table 1 and Figure 2). The northern extension of the first two Africa regions, which is primarily over desert, was designed to find TEBs [*Dwyer et al.*, 2008; *Carlson et al.*,

2011; *Xiong et al.*, 2012]; TGFs are not expected in this area based upon previous TGF observations and the low lightning rate. The exposure is intentionally biased, optimized for geographic regions and seasons in which TGFs are likely. During the selected dates data are collected independent of time of day so that there is no intentional diurnal bias. The TGF detection sensitivity is highest for sources within a few hundred km of the nadir of Fermi (see section 3.2); those locations and the times that they are observed depend on the orbit of Fermi, which shifts with a 53.2 day precession period.

From 26 May 2011 to 31 August 2011, TTE data were collected from two control regions for the purpose of testing the TGF detection process, one in the Southeast Pacific and the other in the Indian Ocean. The northern extensions of the first two Africa regions, designed to find TEBs, also serve as a control region for TGFs (Table 1 and Figure 2). The northern Africa extension covers desert areas and the oceanic control regions are far from land. Lightning and TGFs are rare in these control regions – none of the 274 GBM triggered TGFs through 31 August 2012 and only three of 1012 RHESSI TGFs [*Gjesteland et al.*, 2012] are within these regions. (The events observed by RHESSI on 17 January 2004 and by GBM on 14 December 2009 over northern Africa were TEBs that are geomagnetically connected to sources in southern Africa [*Smith et al.*, 2006; *Briggs et al.*, 2011]). The total data accumulation for the sample of this paper, made over 412 days between 9 July 2010 to 31 August 2011, is 1224.8 hours of TTE divided between 1036.7 hours in TGF-active regions and 188.1 hours in TGF control areas (Table 1). The TTE accumulation in the TGF-active regions is divided into 1029.6 hours of continuous TTE and 7.1 hours of TTE data that are attached to on-board TGF triggers (see section 2.4).

2.2. Search Method and Detection Criteria

The availability of the individual count data makes possible searches using finer time resolution than is available to the flight software. For simplicity we use a binning approach, with sixteen bin widths from 25 μs to 16 ms (Table 2) and four phases so that TGFs and TEBs will be unlikely to be missed regardless of their duration or position with respect to the start of the binning. The TTE data are separately binned for each of the two BGO detectors and the sum of the twelve NaI detectors, resulting in three independent time series with the same time binning. The data of the NaI detectors are merged because a single GBM NaI detector has a much smaller response to a TGF than a GBM BGO detector. For additional details see appendix section A2.

The data of each time bin are tested for a statistically significant excess of counts using the cumulative Poisson probability

$$P(N \geq N_{\rm obs}|R_{\rm background}) = \sum_{N=N_{\rm obs}}^{\infty} P_{\rm Poisson}(N|R_{\rm background}), \quad (1)$$

where $N_{\rm obs}$ is the number of counts observed in the time bin, N is an index of count values and $P_{\rm Poisson}(N|R_{\rm background})$ is the Poisson probability of observing N counts when the counting rate is $R_{\rm background}$. The expected background count rate, $R_{\rm background}$, in counts per bin, is calculated as the average of 5 seconds of data before and 5 s of data after the bin, with a 1 s gap in between. For a time bin with an excess to be classified as a TGF or TEB the following criteria must all be met:

1. The cumulative Poisson probabilities (equation 1) $P_{\rm B0}$ and $P_{\rm B1}$ of each BGO detector must be less than 0.001.

2. The cumulative Poisson probability (equation 1) $P_{\rm NaI}$ for the sum of the NaI detectors must be less than 0.001.

3. Each BGO detector must have at least four counts.

4. The corrected, joint Poisson probability $P_{\rm joint}^{\rm corr}$ must be less than 1×10^{-11} (described below).

5. The excess must not be a digital glitch (described below),

6. The excess must not be identified as a cosmic ray shower according to tests applied to the GBM data (sections 2.3.1 & A3),

7. The excess must not be identified as a cosmic ray shower according to tests applied to the LAT calorimeter data (see sections 2.3.2 & A4).

Requirements 1 and 2 demand a simultaneous signal in each of three "detectors", considering the merged NaI data to be a single detector. Requirement 3 is necessary so that the event is strong enough for reliable classification. The joint Poisson probability of a candidate (requirement 4) is calculated as the product of the three detector probabilities, corrected for the number of time bins $N_{\rm bins}$ in the datafile (typically a pass through a TTE region):

$$P_{\rm joint}^{\rm corr} = 1 - (1 - P_{\rm B0} P_{\rm B1} P_{\rm NaI})^{N_{\rm bins}}. \quad (2)$$

This partially compensates for the large number of time bins that are searched, requiring a high statistical significance of the joint signal of the three independent time series even considering the large number of time bins searched. Figure 3 shows an example detection of a TGF.

The overall probability that a candidate is a chance fluctuation is difficult to determine because, while there are a very large number of trials, there is also a large overlap in the trials because of the multiple bin widths and phases. Additionally the

value $P_{\rm joint}^{\rm corr}$ does not take into account some of the requirements, such as the individual detector probability thresholds (requirements 1 and 2) and the individual BGO count thresholds (requirement 3). For these reasons $P_{\rm joint}^{\rm corr}$ is not precisely the probability that a candidate is a chance fluctuation. Nonetheless the $P_{\rm joint}^{\rm corr}$ values are useful to rank the candidates. Typically candidates are found multiple times, on several bin widths and phases. The $P_{\rm joint}^{\rm corr}$ values are also useful to sort through the multiple times that the same candidate is found by the search: the bin with the most significant (smallest) value of $P_{\rm joint}^{\rm corr}$ is considered to be the "discovery" bin.

Tests were applied to the candidates and the threshold $P_{\rm joint}^{\rm corr} = 1 \times 10^{-11}$ was empirically selected to create a sample that reliably contains TGFs (see appendix section A5). Lightning strokes emit radio waves (sferics) that can be observed at very large distances in Very-Low Frequency (VLF) radio. Networks such as the World Wide Lightning Location Network (WWLLN) use multiple VLF receivers to locate lightning with high temporal and positional accuracy [*Dowden et al.*, 2002; *Rodger et al.*, 2009]. The TGF candidates are correlated with WWLLN locations to find associations [*Connaughton et al.*, 2012]. If $P_{\rm joint}^{\rm corr}$ is set too high, accepting less significant candidates, then the TGF / WWLLN association rate is found to be lower than expected from GBM triggered TGFs, indicating contamination of the sample with non-TGFs (see appendix sections A5 & A6). Additionally LAT data show less significant sub-samples to have higher rates of cosmic-ray contamination (see sections 2.3.2, A5 & A6).

Rare glitches in the time stamps of the TTE data move counts from correct times to incorrect times, doubling the rates for the time interval that contains both true and

time-shifted counts. These spurious candidates are identified by their digital patterns and removed (requirement 5).

2.3. Removal of Cosmic-Ray Showers

2.3.1. Cosmic Rays identified with GBM Data

Briggs et al. [2010] found that very energetic cosmic rays produce showers in Fermi that appear similar to TGFs in GBM. These events are identifiable as cosmic rays in the LAT calorimeter and have several distinguishing characteristics in the GBM data. Weaker cosmic ray showers are found with the offline search that do not satisfy the criteria that were developed to automatically classify GBM triggers as cosmic ray showers, e.g., the number of detectors with simultaneous counts is lower. Improved criteria (see appendix section A3) were developed to identify cosmic ray showers based upon their characteristics in the GBM data and are used to automatically remove cosmic ray showers from the sample (requirement 6). The number of candidates removed is large but uncertain because duplicate candidates (bin widths and phases) were not merged into unique events before removing them.

2.3.2. Cosmic Rays identified with LAT Data

In *Briggs et al.* [2010] large energy depositions in the LAT calorimeter were used to show that two GBM triggers that appeared similar to TGFs were actually cosmic ray showers. Events like these and many weaker ones are now automatically removed from the sample using their GBM characteristics. However, the criteria that filter out cosmic ray showers using the GBM data were designed to retain TGFs at the expense of not removing all cosmic ray events. To remove the remaining cosmic ray events, we again use the LAT calorimeter data. For each candidate, the individual events of the

calorimeter data stream are examined around the time of the discovery bin, starting from 0.1 ms before the start of that bin to 0.1 ms after the end. A subset of the candidates has a LAT event during this interval with the morphology of a hadronic shower and depositing > 10 GeV in the calorimeter – indeed, typically > 60 GeV. Such energies appear impossible for a thunderstorm to produce based on the electric potentials of thunderstorms [*Marshall and Stolzenburg*, 2001], so such measurements indicate a cosmic ray origin for these candidates. These cosmic ray events are removed from the sample (requirement 7).

Appendix section A4 explains additional details of event readout of the LAT data, the LAT cosmic ray filter, and leakage past the filter.

2.4. The Sample and its Reliability

To define a sample of candidate TGFs, separate discovery bins (pulses) within 1 s of each other are merged and considered to be a single event. For the dataset of this paper this was only done for one event, merging two pulses that are separated by 24 ms.

The sample found in the TGF-active regions (i.e., not including the control region data) is from 1036.7 hours of observations (Table 1). GBM data processing sorts TTE data into "trigger" and "continuous" files depending on whether the data are associated with an on-board trigger or were generated during a TTE region without a trigger, causing these 1036.7 hours of data to be split into 1029.6 hours of continuous TTE files and 7.1 hours of TGF trigger TTE files. The search method and criteria applied to the 1029.6 hours of continuous TTE collected in the TGF-active regions creates a sample of 384 previously undetected TGFs. If the TTE data associated with on-board TGF triggers that occurred when Fermi was within TTE-collection regions were omitted the

sample would be biased against the bright TGFs and TEBs that were already detected on-board by the flight software. The offline search applied to the 7.1 hours of TGF-trigger TTE contained in the TGF-active regions "rediscovers" all 41 of the triggered TGFs and TEBs. The least significant trigger is detected at $P_{\rm joint}^{\rm corr} = 3 \times 10^{-54}$; none have a high-energy deposition in the LAT calorimeter. (There were no TGF triggers in the control regions during the time periods. Less than 1% of the time that Fermi was within the regions was excluded from the exposure time because TTE data from non-TGF triggers was not included in the search.) Using the TGFs found in both types of TTE files creates a unified sample of 425 TGFs and TEBs obtained during 1036.7 hours of observing time in the TGF-active regions.

With 425 TGFs in the TGF-active regions and only one in the control regions, the detection rates are 0.41 TGFs per hour and 0.005 per hour, respectively. This shows the effectiveness of the search method and filtering criteria, which find TGFs at a more than $\times$70 higher rate in regions where they are expected than in control regions where they should be extremely rare. In our final sample we omit the candidate in the control region as doubtful based on its location.

The 41 triggered events include two TEBs, 110410.216 and 110625.474 [*Xiong et al.*, 2012], which are most significant on the 8 and 4 ms bin widths, respectively. These two are firmly classified as TEBs based upon their durations, time histories, preferential detections on one side of Fermi and observations of lightning with WWLLN at a magnetic footprint. Two other triggered TGFs are most significant on long bins, 2 ms in each case, but the WWLLN lightning observations are more consistent with a nadir source location and thus a gamma-ray detection. Eight of the 39 triggered TGFs have

associations with WWLLN lightning locations, as does one of the two TEBs; this is consistent with the expected rate.

The association rate with WWLLN locations of the final sample of 384 TGFs found in the continuous TTE by the offline search is 35%, which is higher than the value of 27.6% expected from GBM triggered TGFs (triggered sample described in appendix section A5). The two samples are most consistent with a common association rate of 33.0%, giving a consistency probability of 2% (probability method described in appendix section A5). There are several possible reasons for the marginally inconsistent association rates. The divergence from a common association rate might be a chance fluctuation in one or both samples. *Connaughton et al.* [2012] show the TGF / WWLLN association rate to correlate with TGF duration, which will cause the two samples to have different association rates since the two samples have different duration distributions (see section 3.3). Additionally the exposure time of the continuous TTE sample, compared to the triggered sample, is biased towards the Americas region (Table 1 and Figures 2), where WWLLN has a high detection efficiency due to a high density of VLF receivers [*Rodger et al.*, 2009; *Hutchins et al.*, 2012]. Even with these reasons for differing GBM / WWLLN association rates, the high association rate for the continuous TTE sample shows that it contains at most a few non-TGFs.

In appendix section A4 we estimate the contamination of the sample with cosmic ray events as ∼2%. Conversely, in that section we estimate that at most two TGFs may have been misidentified as cosmic rays using the LAT calorimeter data, setting an upper limit of 1.3% for the mistaken removal of TGFs from the sample due to this criterion.

2.5. Sample Properties: Search Parameters

Table 2 and Figures 4A, B & E show the properties of the TGFs and TEBs versus discovery bin width. "Discovery bin width" is the width of the search bin for which $P_{\rm joint}^{\rm corr}$ is most significant (smallest) while "discovery counts" are the number of counts in that bin. Discovery counts may include a very small number of background counts; conversely, there may be additional TGF counts outside of the discovery bin. Discovery bin widths for TGFs range from 35 μs to 2 ms. Additionally the two triggered TEBs are best found by the offline search at 4 and 8 ms. No events were found at the shortest and longest bin widths used in search. Most of the TGFs were found between 70.7 and 632 μs. There is a trend for the envelope of the discovery counts to increase with the width of the discovery bin (Fig. 4A). The trend could either indicate that short TGFs have less fluence or that the GBM detectors are unable to accumulate a larger number of counts in the shorter bins due to deadtime (see section 3.3).

The pattern for $P_{\rm joint}^{\rm corr}$ versus discovery bin width, shown in Figure 4B, is more complex. The eleven TGFs found in the 35 and 50 μs bins are less significant due to their smaller number of counts. $P_{\rm joint}^{\rm corr}$ values range from 9.7×10^{-12}, just below the threshold of 1×10^{-11} of requirement 4, to three that are below 1×10^{-300}. Figure 4C shows $P_{\rm joint}^{\rm corr}$ values versus discovery counts; Figure 4D a histogram of discovery counts. These two parameters are highly correlated with only a few outliers, including both TEBs in the sample. The discovery counts for TGFs found only with the offline search range from 16 to 194 with a median of 50. The values for the triggered TGFs and TEBs ranging from 73 to 748, so that the values for the two groups overlap. TGFs found with the offline search must have at least 8 counts in the BGO detectors due to requirement 3. They will have additional counts in the NaI detectors due to requirement 2 – the

lowest value in the sample was 8, spread over the 12 NaI detectors. At the threshold $P_{\rm joint}^{\rm corr} = 1 \times 10^{-11}$ most of the TGFs have discovery counts between 20 and 38 (Figure 4C). Ideally the threshold of a sample would be set in physical units; for this sample it is set by a probability calculation that leads to a broad range of detected counts. The effective threshold for detection in discovery counts (50% level) is about 25 (Fig. 4D). This value is higher than that of some other TGF samples, showing the conservative nature of the GBM offline-search criteria. For example, the original offline search of the RHESSI data [*Grefenstette et al.*, 2009] has an effective threshold of about 15 counts (Fig. 8 of *Collier et al.* [2011]), while the revised search has an effective threshold of about 10 counts (Fig. 2a of *Gjesteland et al.* [2012]). The AGILE TGF criteria require at least 10 counts [*Marisaldi et al.*, 2010a]. Statistical significance also depends on the background levels of the instruments.

423 TGFs and 2 TEBs were found in 1036.7 hours of observations, for a TGF detection rate of 0.41 hour^{-1}, which is an unprecedented TGF detection rate. These observations were, however, conducted over regions and during seasons selected for their known high TGF activity. A simple measure of the increase in sensitivity that takes into account these biases is that the ratio of the additional TGFs found with the offline search to the TGFs detected with the on-board triggering method during the 1036.7 hours is larger than nine.

3. Results

3.1. Source Locations

Figure 5 shows the locations of Fermi (nadirs) at the times of the 425 TGFs and TEBs. Also shown are the boundaries of the regions in which the data were collected

and the geographic distribution of the observation time. There is higher exposure near the latitude extremes of the orbit, which results in an oversampling of TGFs at high latitudes and the creation of artifacts on the map, such as the row of TGF detections near Florida at the latitude limit of the orbit. This concentration of spacecraft locations results from the combination of higher exposure at high orbital latitudes and high TGF source concentrations near Florida, the Bahamas and Cuba. Figure 5 is the typical TGF / TEB geographical figure, showing the positions of the spacecraft at the times of the TGFs and TEBs.

With this large TGF sample and the large fraction of GBM TGFs that have geolocations of $\approx$ 10 km accuracy from WWLLN [*Abarca et al.*, 2010], it is useful to map instead the source locations (Fig. 6). These maps more clearly display geographical and meteorological patterns since the smearing caused by the nadir-source separations is removed. A preference towards coastal regions [*Hazelton*, 2009; *Smith et al.*, 2010] is strongly evident, described by *Splitt et al.* [2010] as "TGF occurrences are frequent near coastlines, large islands, peninsulas, and isthmuses in the tropics where low level atmospheric convergence is often enhanced and promotes thunderstorm development". This coastal enhancement corresponds to the higher lightning density observed by WWLLN for coastal regions [*Virts et al.*, 2012]. In Figure 6A there is a very strong concentration at and in the vicinity of Cuba, which is the result of the intrinsic TGF activity of Cuba and the increased exposure near the latitude extremes of Fermi's orbit. Figure 7A shows how the locations of Fermi for these TGFs "move" to the source locations. Two of the spacecraft locations in the apparent row near Florida (Fig. 5A) result from TGFs above the latitude limit of the orbit, in or near Florida, while most of

the rest originate from TGFs from Cuba. The map of Australia (Fig. 6C) shows an extreme coastal pattern, with Fig. 7C showing how some of the sources were observed when Fermi was above the desert interior.

Not all of the TGFs are coastal. The TGFs that are farther from the coasts of Mexico and Central America are likely from storms of the Intertropical Convergence Zone (Fig. 6A). Africa has both coastal and interior TGFs (Fig. 6B).

3.2. Source-Nadir Offset and Diurnal Distributions

Figure 8A shows the distribution of offsets between the nadirs and WWLLN locations of the 141 TGFs with WWLLN associations. The offsets reach up to ∼800 km (54°) with a median of 360 km (34°). Up to 300 km (30°) the number of TGFs is consistent with the observed area, which agrees with a uniform TGF density combined with a detection efficiency that is independent of offset. Past 300 km the number quickly falls below the area curve, indicating a change past this offset of TGF characteristics as observed with GBM. The low value in the bin 300–350 km is unlikely to be physical because of the narrowness of the apparent dip; instead the low value is mostly likely a statistical fluctuation with probability $P \approx 0.01$ to occur in a particular bin, or $P \approx 0.1$ to occur in some bin. Previously GBM triggered TGFs were all found to be within 300 km (30°) of the nadir, with a median of 200 km (21°) [*Connaughton et al.*, 2010]. The sample of this paper has a single triggered TGF past 300 km, at an offset of 660 km (49°). This outlier may be a rare exception to the findings of *Connaughton et al.* [2010] or this particular GBM / WWLLN association might be due to chance [*Connaughton et al.*, 2012]. Previous observations of the TGF offset distribution are summarized by *Connaughton et al.* [2010] and by *Collier et al.* [2011].

Figure 8B shows the GBM TGF offset distribution as rate density. The rate is based upon the total observation time of 1036.7 hours and the area calculation uses a spherical earth [*Gjesteland et al.*, 2011]. The GBM / WWLLN measurements of nadir-source offsets are corrected to GBM rate density by dividing by the GBM / WWLLN association rate of 0.334. The observations are consistent with a constant rate of 6×10^{-7} GBM TGFs hour^{-1} km^{-2} from 0 to 300 km. The RHESSI TGF density [*Collier et al.*, 2011], obtained with the first search method [*Grefenstette et al.*, 2009], peaks at $\sim 2.5 \times 10^{-8}$ TGFs hour^{-1} km^{-2}. (We use results from the original, less sensitive RHESSI search because of the availability of a TGF offset distribution figure for 93 RHESSI TGFs, Fig. 6b of *Collier et al.* [2011]. The peak RHESSI rate density is estimated from that figure by converting 180 TGFs Mm^{-2} as the maximum over 100 km width and using 8.5 years of observations and an RHESSI / WWLLN association rate of 9.6%.) Three factors explain the $\sim \times 24$ higher rate density observed with GBM: 1) the GBM sample was collected for seasons and regions selected for their TGF activity, while the RHESSI sample is for all times ($\times 4.2$, section 3.4.1), 2) the RHESSI observations extends to higher latitudes than the GBM orbit, where the TGF rate is lower ($\times 1.65$, [*Smith et al.*, 2010; *Østgaard et al.*, 2012]), 3) with the offline search GBM is more sensitive at detecting TGFs than RHESSI. After accounting for the first two factors, the TGF detection rate ratio between the instruments/searches due to their different sensitivities need only account for $\times 3.5$ of the differences in rate densities. (The RHESSI rate density would be higher and this factor smaller if the rate density from the new search were used – see section 3.4.1 and appendix section B2.)

TGFs observed at small offsets are brighter, on average, since the spacecraft is within the primary beam and there is less atmospheric attenuation (Figure 8C). At larger offsets TGFs are weaker, consisting of Compton scattered photons and subject to greater attenuation [*Østgaard et al.*, 2008; *Hazelton et al.*, 2009; *Collier et al.*, 2011; *Gjesteland et al.*, 2011]. At any offset there are some weak TGFs, e.g., due to the intrinsic strength of the source or greater atmospheric depth. The difference between the two GBM offset distributions can be understood as a result of the improved sensitivity of the offline search. The on-board triggering method is only able to detect the bright primary beams while the offline search is able to detect TGFs that consist of Compton scattered photons at larger offsets.

Figure 9 displays the diurnal distribution of the TGFs by local solar time. The distribution has the highest rate in the afternoon hours of 14:00 to 18:00 and the lowest rate before noon. The agreement with the diurnal distributions found for large samples of RHESSI TGFs [*Hazelton*, 2009; *Splitt et al.*, 2010] is another confirmation that this sample consists predominantly of TGFs.

3.3. Durations

Figures 10A and 10B show the distributions of the t_{90} and t_{50} duration measures, respectively, for 425 pulses from the 423 TGFs of the sample. The t_{90} value is the length of the interval in which 90% of the counts are accumulated, with 5% of the counts occurring before and 5% after this interval; similarly the t_{50} interval contains 50% of the counts, with 25% before and after [*Briggs et al.*, 2010]. When there are separated pulses, we determine t_{90} and t_{50} for each pulse. (This is different from GRBs, for which single values of t_{90} and t_{50} are determined per GRB, including any inter-pulse gaps.) Two

TGFs had separated pulses in this sample. The median of the t_{90} values for the entire sample of 425 pulses is 240 ± 25 μs; of the t_{50} values, 100 ± 10 μs (the errors are determined via bootstrap analysis). The t_{50} median is consistent with the t_{50} median of 110 μs of an earlier sample of 48 pulses from 45 triggered GBM TGFs [*Fishman et al.*, 2011].

The offline search of the continuous TTE finds shorter TGFs than are found by the onboard trigger. (Figures 4E & 10A & B). The error of the median is very large for small samples, likely because the duration distributions are very broad, so the median is ill suited for testing whether two distributions are different. Instead the consistency of the duration distributions of the continuous TTE and triggered TGFs are tested with the two-sample Kolmogorov-Smirnov (KS) test. The two-sample KS test applied to the observed t_{50} distributions (39 triggered pulses and 386 continuous TTE pulses) finds that they are from different distributions at the 99.8% confidence level. Similarly the KS test finds the observed t_{90} distributions to be drawn from different distributions at the 99.6% confidence level. Expanding the triggered TGF sample to the 184 triggered TGFs between 28 August 2008 and 28 August 2011, the confidence levels that the triggered TGFs and the TGFs found in the continuous TTE are from different distributions increases to better than 99.99% for both t_{50} and t_{90}. (The t_{50} and t_{90} measurements for these samples have duplicate values because the data are binned at 10, 20 or rarely 40 μs resolution to determine these duration measures; the existence of duplicate values in the sample was considered in calculating the chance probabilities of the observed KS statistics [*Nikiforov*, 1994] (`http://lib.stat.cmu.edu/apstat/288`).) The difference is observational, with likely several causes. The offline search applied to the continuous

TTE data is able to detect shorter TGFs than the on-board triggering method. Conversely, the offline search is finding TGFs further off-axis than the on-board method and these TGFs will tend to be longer due to Compton scattering.

Very few TGFs were detected on the shortest times scales, i.e., were most significant in the search for discovery bin widths of 35 and and 50 μs (Figure 4E & Table 2). These widths are only $\times$13 and $\times$19 longer than the GBM deadtime per count (2.6 μs), so perhaps deadtime is limiting the ability of GBM to detect these TGFs. If a TGF produces a count in the overflow channel, which imposes a 10.4 μs deadtime, the deadtime is even closer to the search bin width. To test this idea, Figure 11 compares the fractions of the discovery bins lost due to deadtime in the BGO detectors for two duration groups: the shortest TGFs by discovery bin width and those of the discovery bin width in which the most TGFs were found. The first group is defined as the two TGFs that were most significant on the discovery bin width of 35 μ and the nine that were most significant on the bin width of 50 μs. The comparison group comprises 109 TGFs that were most significant on the bin width of 141 μs (Table 2). The deadtime fraction in each BGO detector ($x = 0, 1$) is calculated as

$$f_{\mathrm{BGO}x} = \frac{1}{\Delta}(N_{\mathrm{reg}}\, 2.6\ \mu\mathrm{s} + N_{\mathrm{ovf}}\, 10.4\ \mu\mathrm{s}) \tag{3}$$

where Δ is the width of the discovery bin in μs, N_{reg} is the number of regular (non-overflow) counts in the discovery bin for that BGO detector and N_{ovf} is the number of overflow counts. This equation gives the fraction of the discovery bin for which the GBM electronics are unable to register another count because of the proximity of the preceding count. The counts N_{reg} and N_{ovf} are not the discovery counts of the offline search – they include all counts, not just those of the energy channels used in the search

(appendix section A2). The deadtime fraction used in Figure 11 is the larger of $f_{\rm BGO0}$ and $f_{\rm BGO1}$. While there is some overlap between the two groups, Figure 11 shows the very short TGFs to have on average have higher deadtime fractions than the 141 μs group. (None of the TGFs reach 100% deadtime; due to the Poisson arrival of the photons, intervals longer than the deadtime are likely between some pairs of photons unless the intensity is extremely high and the detector is totally saturated.) The two-sample KS test gives a probability of 0.023 that the two distributions result by chance from the same parent distribution, indicating that they are different at modest significance. (The comparison of the distributions is limited by the small size of the very short TGF sample.) This strongly suggests that instrumental deadtime is reducing the ability of GBM to detect the shortest TGFs. For these very short TGFs, for which the GBM deadtime per count of 2.6 μs is not much smaller than their durations, it is difficult for GBM to accumulate enough counts to achieve statistical significance and to meet the search requirements. This suggests that instrumental biases are causing undersampling of the short end of the duration distribution (Figures 4E & 10A & B).

Figure 10C shows the distribution of counts contained in the t_{90} intervals of the pulses. This figure has similarities with Figure 4D, with the TGFs found in the offline search typically having fewer counts, but the high-count tail of these TGFs substantially overlapping with the distribution of the triggered TGFs.

Numerous definitions of TGF duration have been used. This paper uses three: discovery bin width, t_{50} and t_{90}. Comparisons with the observations of other instruments are difficult due to the use of differing methods of measuring TGF durations. *Nemiroff et al.* [1997] made duration estimates for 13 BATSE TGFs based upon subjectively

estimating their starting and stopping points. One definition is $\pm 2\sigma$ from a Gaussian fit to the count time history, used for BATSE by *Gjesteland et al.* [2010] and for RHESSI by *Østgaard et al.* [2012]. AGILE uses the length of consecutive bins that have counts, extended past a single-bin gap if the next bin has a high-energy count [*Marisaldi et al.*, 2010a]. Figure 12A compares the t_{90} and t_{50} values for the GBM sample; while t_{90} is obviously larger than t_{50} for each TGF there is a reasonably close correlation between the two. (Due to binning of the data one short TGF has equal t_{50} and t_{90} values.) *Fishman et al.* [2011] found an average ratio of 2.48 between the two; this sample has a mean ratio of 2.32 and a median ratio of 2.17. Discovery bin width and t_{90} are less closely correlated (Fig. 12B). Discovery bin width is shorter than t_{90} for 75% of the TGFs, likely because a shorter interval can maximize significance by improving the signal-to-background ratio. The counts in the discovery bin and in the t_{90} interval are closely correlated (Fig. 12C), but because the discovery bin width tends to be shorter than t_{90} the discovery counts tend to be fewer than the t_{90} counts (77% of the TGFs).

3.4. TGF Rate and Lightning

The comparison between the 39 TGFs and 2 TEBs detected on-board by the flight software and the 384 TGFs found by searching the TTE data on the ground clearly shows the increased sensitivity of the offline search method, primarily due to searching shorter intervals than 16 ms. However, the intentionally biased sampling of the continuous TTE data, which were collected in TGF-active regions and seasons, means that analysis is required to deduce the unbiased TGF rate. To overcome the non-uniform sampling of the GBM data we normalize the GBM TGF observations to a lightning dataset that has more uniform geographic and seasonal sampling than the

gamma-ray observations of this paper. As was done in prior TGF analyses [*Smith et al.*, 2010; *Fuschino et al.*, 2011; *Østgaard et al.*, 2012], we use the data of the Optical Transient Detector (OTD) (operational on MicroLab-1 from 1995–2000) and the Lightning Imaging Sensor (LIS) (operational on TRMM from 1997), both of which are spaced-based optical lightning detectors [*Boccippio et al.*, 2002; *Christian et al.*, 2003]. GBM views to the Earth's horizon at 2500 km but only detects TGFs within ~ 800 km of the nadir of Fermi (Fig. 8). LIS has a field of view of 600×600 km. With these small fields of view in instruments with different orbits the probability of a simultaneous observation of a GBM TGF and an associated LIS lightning flash is very low; here we only compare the rates. The annualized LIS/OTD maps are created from the narrow-field observations, accounting for detection efficiency and diurnal and seasonal variations in the lightning rate, to produce gridded exposure maps with flash rate in units of $\mathrm{km}^{-2}\ \mathrm{year}^{-1}$. The exposure correction is for overall flash detection efficiency, based on observations made with a U2 aircraft that determined the radiant energy threshold for a 90% detection efficiency [*Boccippio et al.*, 2002; *Christian et al.*, 2003]. To match the concept of a lightning "flash", the flash rates in the maps are based on merging pixels using a clustering algorithm with scales of 5.5 km and 330 ms [*Mach et al.*, 2007]. However, our method of normalizing the GBM TGF observations using lightning data has the limitation that the TGF / LIS-lightning ratio is known to vary geographically [*Smith et al.*, 2010; *Fuschino et al.*, 2011].

The rate, R_{GBM}, of TGFs detected by GBM when Fermi is at latitude λ_{GBM} and longitude ϕ_{GBM} is

$$R_{\mathrm{GBM}}(\lambda_{\mathrm{GBM}}, \phi_{\mathrm{GBM}}) = \int dA\, \epsilon(\rho) R_{\mathrm{TGF}}(\lambda_{\mathrm{src}}, \phi_{\mathrm{src}}) \tag{4}$$

where the integration is over areas dA with sources at latitudes λ_{src} and longitudes ϕ_{src}, $R_{\mathrm{TGF}}(\lambda_{\mathrm{src}}, \phi_{\mathrm{src}})$ is the TGF rate above GBM's intensity threshold, with units of km^{-2} s^{-1}, and $\epsilon(\rho)$ is the GBM detection efficiency as a function of offset ρ (km or degrees) from the nadir, defined as unity at the nadir. The intrinsically faintest TGF detectable by GBM has a particular flux; the rate above this flux is R_{TGF}. As a function of offset ρ GBM can only detect intrinsically brighter TGFs, with a lower detection rate caused by factors such as the TGF intensity beam pattern, TGF spectral properties across the beam and increasing atmospheric absorption at larger observation angles, resulting in a detection efficiency $\epsilon(\rho)$. Azimuthal symmetry in the detection of TGFs is assumed so that ϵ depends only on the offset ρ between the nadir $(\lambda_{\mathrm{GBM}}, \phi_{\mathrm{GBM}})$ and source position $(\lambda_{\mathrm{src}}, \phi_{\mathrm{src}})$.

Integrating over the observing times t corresponding to when GBM is located over a geographic region Ω, the expected number of TGFs detected in that region is

$$N_{\mathrm{GBM}}(\Omega) = \int dt \int dA\, \epsilon(\rho) R_{\mathrm{TGF}}(\lambda_{\mathrm{src}}, \phi_{\mathrm{src}}), \tag{5}$$

The offset ρ is implicitly a function of the integration variables. Further assuming that a fraction $f_{\mathrm{T/L}}$ of LIS/OTD lightning flashes are associated with TGFs above GBM's intensity threshold:

$$N_{\mathrm{GBM}}(\Omega) = f_{\mathrm{T/L}} \int dt \int dA\, \epsilon(\rho) R_{\mathrm{LIS}}(\lambda_{\mathrm{src}}, \phi_{\mathrm{src}}), \tag{6}$$

where $R_{\mathrm{LIS}}(\lambda_{\mathrm{src}}, \phi_{\mathrm{src}})$ is the LIS/OTD lightning flash rate (units: km^{-2} s^{-1}).

As shown with the grey scales on Figure 5, the observing times of the TTE data have been accumulated into approximately 1° square pixels by the locations of Fermi. Similarly we use 0.5° gridded LIS/OTD data (High Resolution Annualized Climatology and High Resolution Monthly Climatology, `http://thunder.msfc.nasa.gov/data/index.html`). Using these binned datasets, equation 6 becomes a double sum over the bins of the GBM exposure map and the bins of LIS/OTD lightning rate map to predict the number of GBM TGFs for some region or observing period (e.g., the entire sample of this paper, or a particular TTE collection region):

$$N_{\mathrm{GBM}} = f_{\mathrm{T/L}} \sum_i t_i \sum_j \Delta A_j \epsilon(\rho) R^j_{\mathrm{LIS}}, \tag{7}$$

where the sums are over the bins i of the GBM exposure map contained in that region (Fig. 5) and bins j of the LIS/OTD data set, t_i is the GBM exposure in bin i (units: s), R^j_{LIS} is the LIS/OTD lightning rate in bin j of the LIS/OTD data set (units: flashes km^{-2} year^{-1}), and ΔA_j is the area of LIS/OTD pixel j (units: km^{-2}). A value of ρ is implicit for each pair of GBM exposure bin i and lightning map bin j.

To obtain the GBM detection efficiency $\epsilon(\rho)$ as a function of offset ρ we use an empirical function to smooth the data. Since the observations are consistent within their errors with a uniform density of detected TGFs to 300 km (cf. data to area histograms in Figure 8A), we model the detected TGF density with a uniform density to 300 km and decreasing density at larger offsets (Fig. 8B). We use the shape of this empirical curve for $\epsilon(\rho)$, normalizing to $\epsilon(0) = 1$. This leaves the TGF / lightning ratio $f_{\mathrm{T/L}}$ as the sole unknown quantity. Solving equation 7 we obtain $f_{\mathrm{T/L}} = (3.8 \pm 0.2) \times 10^{-4}$, indicating a ratio of $\approx \frac{1}{2600}$ between TGFs above GBM's intensity threshold and

LIS/OTD lightning flashes. However, we confirm that the ratio between TGFs and lightning varies geographically [*Smith et al.*, 2010; *Fuschino et al.*, 2011], with lightning in Africa and Asia being relatively ineffective compared to lightning in the Americas in producing TGFs and lightning in Australia being more effective (Table 3).

The LIS/OTD data are exposure corrected to overall flash rate [*Boccippio et al.*, 2002; *Christian et al.*, 2003]. TGFs are very likely associated with IC lightning [*Williams et al.*, 2006; *Stanley et al.*, 2006; *Shao et al.*, 2010; *Lu et al.*, 2010; *Cummer et al.*, 2011], so the ratio between TGFs and IC lightning would be more useful rather than the all-lightning ratio. *Boccippio et al.* [2001] find the ratio IC/CG to be 2.64–2.94 (or $\frac{\mathrm{IC}}{\mathrm{IC+CG}} \approx 0.74$) for the continental US, but with very large variations. *Østgaard et al.* [2012] used the average IC/CG ratio for the continental US to correct the observed RHESSI TGF / LIS lightning ratio to a ratio for IC lightning, obtaining 9.8×10^{-5}. While *Boccippio et al.* [2001] assume that OTD had equal detection efficiencies for IC and CG lightning, there is a possibility that space-based optical sensors might have higher detection efficiencies for IC lightning than for CG. Because of these uncertainties we choose not to correct the ratio $f_{\mathrm{T/L}}$ from all lightning to IC lightning.

3.4.1. GBM Annual TGF Rate

By assuming that the measured values of $f_{\mathrm{T/L}}$ can be extended to larger regions we can use the LIS/OTD observations to predict how many TGFs GBM would detect if TTE data were collected for the entire orbit of Fermi, excluding the South Atlantic Anomaly (SAA) region. This approach is approximate because the TGF / lightning ratio $f_{\mathrm{T/L}}$ varies geographically, but should achieve a good estimate since GBM data have already been collected over the regions with the highest TGF activity, which make

the largest contributions to the total, and Fermi does not reach the higher latitudes where TGF rate per lightning is appreciably lower [*Smith et al.*, 2010]. We divide the area under Fermi's orbit into four sections and for each section average $f_{\mathrm{T/L}}$ over the TGF-active regions that were observed inside of that section. For the GBM exposure we used the actual exposure for the year 2010, thereby accounting for orbital effects and the detectors being off in the SAA. Using eq. 7 we estimate that with complete TTE production for Fermi's orbit, minus the SAA, GBM would detect ≈850 TGFs per year.

Using preliminary results of the GBM offline search (see appendix section B1), *Østgaard et al.* [2012] used the ratio between the numbers of TGFs found with the offline search of the continuous TTE from selected regions to the TGFs found in-orbit by triggering to calculate how many TGFs GBM would detect with continuous production of TTE data, obtaining 2.5 ± 0.5 TGFs per day, or 900 ± 450 per year. This analysis assumed that the detection ratio between the two detection methods observed for 0.39 of the year and in the selected regions for which the continuous TTE was collected extrapolates to the entire year and the entire area under the orbit of Fermi [*Østgaard et al.*, 2012]. The value from this calculation is consistent with our estimate of ≈850 TGFs per year, an estimate which compensates for the biased observations by normalizing to the LIS/OTD lightning data.

The prediction of ≈850 TGFs per year corrects the observed detection rate of 0.41 TGFs hour^{-1} achieved with selective observations to a predicted unbiased detection rate of 0.097 TGFs hour^{-1} or 2.3 per day. The rate enhancement obtained by collecting continuous TTE for TGF active regions and seasons is ×4.2. In comparison, GBM's detection rate via on-board triggering is one TGF per 4.0 days (based on two years of

observation after the trigger algorithm improvement). BATSE only triggered on TGFs once per 43 days (`http://gammaray.nsstc.nasa.gov/batse/misc/triggers.html`) with its long trigger accumulations of 64 ms or longer. The benefits of reducing the accumulation interval for detecting TGFs are clear. AGILE detects 0.33 TGFs per day, with a relaxed criteria in development that may increase the rate by more than 50% [*Fuschino et al.*, 2011; *Marisaldi et al.*, 2011]. The revised RHESSI search has a detection rate of 0.92 TGFs per day for 2004–2006 [*Gjesteland et al.*, 2012]. The GBM offline search is predicted to have a detection rate $\times 2.5$ higher than RHESSI had when its detectors were in prime condition [*Grefenstette et al.*, 2009]; $\times 1.65$ of this difference is due to Fermi GBM observing a smaller latitude range that has a higher TGF rate ([*Smith et al.*, 2010; *Østgaard et al.*, 2012]), leaving $\times 1.5$ as the rate increase due to sensitivity differences. (Appendix section B2 has additional GBM/RHESSI comparisons.) The annual rate prediction shows that when continuous TTE becomes available for the entire orbit, GBM will have the highest detection rate of any space-based instrument. The higher detection rate is the result of lowering the detection threshold and finding shorter TGFs.

3.4.2. Global TGF Rate

Even with continuous TTE production many TGFs will be unobserved by GBM. TGFs past 1000 km are never detected by GBM and TGFs past several hundred km from the nadir are detected with lower efficiency due to factors such as the TGF intensity and spectral beam profiles, increased atmospheric absorption, etc. The combination of the LIS/OTD lightning data, which is corrected for exposure to report the annual flash rate, and our determination of TGF / lightning ratios $f_{\mathrm{T/L}}$ allows the

calculation of the global TGF rate above GBM's most sensitive threshold. Using the LIS/OTD flash data and the values of $f_{\mathrm{T/L}}$ for the four regions we estimate the overall TGF rate above this threshold and underneath Fermi's orbit (inclination 25.6°) as $(4 \pm 0.2) \times 10^5$ per year. The statistical error is estimated from the numbers of GBM TGFs in each of the four geographic regions; however, systematic errors such as geographic variations of $f_{\mathrm{T/L}}$ are likely as important.

3.5. GBM Annual TGF Rate from Random TTE Data

Here we use a different GBM TTE dataset to independently estimate the annual GBM TGF rate that will be achieved when TTE data are collected at all times instead of for selected regions. This dataset has the advantage of being geographically and temporally random and therefore avoids many of the systematics of the previous estimate, but the amount of data is much smaller so the statistical uncertainty is much larger. The dataset is the TTE data acquired from on-board gamma-ray burst (GRB) triggers. GRBs occur at random times and therefore GRB trigger data is collected at random geographic locations and seasonal times. Typically TTE data are available for ≈ 30 s before the rate increase that initiated a trigger and 300 s after. Triggering is suppressed after a trigger until all special data modes end at ≈ 600 s post-trigger.

The detector rates from GRBs typically do not meet all of the criteria of the offline TGF search and so GRBs are usually not found by the search. Reasons include: 1) Most GRBs, as observed with GBM, have t_{90} durations between 0.1 and 150 s [*Paciesas et al.*, 2012], much longer than TGFs, and may not be significant on timescales $\leq$16 ms. 2) The mean energies of GRBs are lower and so GRBs usually do not produce signals in both BGOs. 3) GBM commonly triggers on GRBs using rates averaged over 50–300 keV

and GRBs may not be statistically significant when averaged over the wider energy ranges used in the TGF search. Occasionally the offline search detects GRB flux, especially near the trigger time. To reduce the effort of manually removing GRB pulses found by the search, data within ±1 s of trigger time were omitted from the search. Even when the offline search does not detect a GRB, GRB flux will increase detector rates for some time intervals and may reduce the sensitivity for detecting TGFs.

The offline search was applied to the TTE acquired from 952 GRB triggers from July 2008 through the end of August 2012 (several triggers are omitted due to missing data). A total of 86.95 hours of TTE were searched, averaging 329 s per trigger. A few triggers had substantially longer TTE coverage. From this search seven TGFs were found meeting all seven requirements (see Figure 13), with $P_{\rm joint}^{\rm corr}$ values ranging from 1.5×10^{-12} to 1.5×10^{-114} and discovery bin widths from 70.7 to 400 μs. Two TGFs occurred before the GRB trigger that generated the data and so did not cause a trigger; we estimate that the other five are insignificant on the 16 ms timescale and would not have caused triggers even if triggering had not been suppressed because of the GRB triggers that preceded the TGFs.

Four of the TGFs are at typical locations: two in southern Africa and two close to large Pacific Islands (Fiji and New Guinea). One is in the Atlantic, 900 km from the Cape Verde Islands. WWLLN data show a storm to the northwest, with numerous lightning strokes extending from 200 km so a smaller offset than 900 km is very likely (Figure 14). Two are in unusual locations. The event in Egypt occurred with Fermi over desert. WWLLN shows clusters of lightning extending southward starting from 800 km; because of this, this event remains barely consistent with being a TGF. The event in the

Indian Ocean occurred when the nadir of Fermi was 1200 km from land. WWLLN shows a single cluster of lightning just past 800 km. This event starts with eight counts that are simultaneous to the 2 μs resolution of GBM. While neither BGO count is in the overflow channel, causing the pattern not to satisfy the GBM cosmic ray filter (appendix section A3), the simultaneous start is suggestive of a cosmic ray. On balance, this event is probably a cosmic ray. The search resulted in five certain TGFs, one uncertain event, and an event that is likely a cosmic ray.

Using the lower number (five), the GBM annual TGF rate should be 440 ± 200; using six TGFs the prediction becomes 530 ± 220. These values are calculated using the ratio of 86.95 hours in this dataset to the hours in a year, with a 86.3% observation factor due to the SAA. The uncertainties are from the Poisson fluctuations on 5 or 6 events.

We test the consistency of these two predictions with the prediction of 850 TGFs per year from the TTE data of the TGF-active regions by calculating the Poisson probability of observing 5 or 6 events assuming that this rate is correct. Because the action-region TTE dataset is so much longer, the statistical uncertainty on its rate is unimportant in the comparison. For an annual rate of 850 (with 86.3% on time), the expected number of TGFs in 86.95 hours is 9.8. Assuming this rate, the probability of observing 5 or fewer TGFs is 0.14; of 6 or fewer is 0.24. These probability values are reasonable and so the annual GBM TGF rate predicted from the GRB TTE data is consistent with the rate estimated with the TTE data collected in the TGF-active regions.

The test of the LAT calorimeter data for high energy depositions identified six candidates in the GRB TTE data as cosmic ray showers that would have otherwise appeared to be TGFs. In comparison, the LAT cosmic ray test removed 41 candidates

from 1217.7 hours of continuous TTE of the TGF-active regions and control regions at $P_{\rm joint}^{\rm corr} \leq 1 \times 10^{-11}$ (Tables 1, 4 & 5), for a removal rate of 0.0337 cosmic rays per hour. This predicts that the LAT test would remove 2.9 cosmic rays from this sample (86.95 hours), compared to the 6 that were removed. Based on the cumulative Poisson distribution, the probability of obtaining 6 or more cosmic ray events when 2.9 are expected is 7.4%, so the prediction and observation are consistent. The predicted residual contamination is 15% (section A4), for about 0.5 cosmic ray events to contaminate the sample. The likely cosmic ray event found when Fermi was over the Indian Ocean is consistent with this prediction. The ratio of cosmic ray events to TGFs is higher for this sample than for the continuous TTE sample because the later sample was collected for regions and times known to have high TGF activity.

4. Discussion

4.1. Global TGF Rate

The first estimate of the global TGF rate appears to have been made by *Smith et al.* [2005]. They used the RHESSI detection rate of one TGF per 2.1 days and a range of possibilities for the detection radius to extrapolate to an overall rate under RHESSI's orbit (inclination 38°). Assuming isotropic emission and an effective horizon of 1000 km, the prediction was 2 $\times 10^4$ TGFs per year, while assuming a narrow beam of 100 km the prediction was 2 $\times 10^6$ per year. Using a more accurate detection distance of 300 km, *Carlson et al.* [2009] refined this estimate to $\geq 2 \times 10^5$ per year. Since AGILE only observes between latitudes ±2.5°, much less than RHESSI, a different technique is needed – simply scaling the TGF rate by the observed and unobserved areas would not account for variations with latitude. Instead *Fuschino et al.* [2011] normalized the

exposure-corrected LIS/OTD lightning rates to the AGILE TGFs. The combination of the AGILE detection rate of one TGF per three days, the TGF / lightning ratio and the global flash rate of 44 per s [*Christian et al.*, 2003] implies a global TGF rate of 8×10^4 to 2×10^5 [*Fuschino et al.*, 2011]. Using a different approach, *Carlson et al.* [2011] compared the GBM detection rates of TGFs and TEBs and deduced a global TGF rate of 5×10^5 per year; however, there is an instrumental bias on the GBM TEB / TGF ratio that accounts for the high value of the ratio (see section 4.2). ADELE, an aircraft-based instrument, observed one TGF from 123 to 436 lightning flashes that were close enough to produce a detectable TGF. Normalizing to the global lightning rate of 44 per s, the global TGF rate was estimated as five million per year, with an uncertainty of up to an order of magnitude [*Smith et al.*, 2011b]. A model-dependent analysis of the detection rates of RHESSI, GBM and ADELE deduced a global rate within $\pm 38^\circ$ latitude and above 5/600 of the lower threshold of RHESSI of 2×10^7 per year [*Østgaard et al.*, 2012].

These estimates of the global TGF rate span a wide range of values with the bulk of the variations due to the TGF threshold. The better previous estimates for global TGF rates above the detection thresholds of spaced-based instruments are broadly consistent with a global rate of 2×10^5 TGFs per year. Estimates that use ADELE data are based on a much lower threshold since ADELE flew much closer to the thunderstorms than the space-based instruments and therefore derive higher TGF rates. We will therefore limit our comparisons to space-based instruments as having similar thresholds. Since GBM is detecting more TGFs than any other space-based instrument the inferred global rate should be higher, which it is, at $\approx 4 \times 10^5$ per year. The increase is consistent with the $\times 1.5$ sensitivity gain compared to RHESSI (section 3.4.1). Perhaps this is partially

chance since the calculation methods are also different. Our TGF / lightning ratio calculation has the improvement of considering the detection efficiency $\epsilon(\rho)$ as a function of offset ρ which appears to produce lower TGF rate estimates then simpler ratio calculations. For example, if we instead approximate that GBM uniformly detects TGFs to $\rho_{\max} = 300$ km and none beyond this radius, the global rate estimate between $\pm 26^\circ$ latitude becomes $\approx 9 \times 10^5$ per year.

The true total global rate is higher because of TGFs below the threshold of GBM. It is very likely that GBM detects weaker TGFs but they are difficult to reliably distinguish from cosmic ray showers. The threshold $P_{\text{joint}}^{\text{corr}} = 1 \times 10^{-11}$ was set by the need to reliably classify events.

While the detection rate of the weakest TGFs might slightly decrease east of the SAA due to increased background (i.e., to achieve $P_{\text{joint}}^{\text{corr}} \leq 1 \times 10^{-11}$ TGFs need a higher counting rate to compensate for the higher background counting rate), the geographic variation of the TGF / lightning ratio (Table 3) appears to be mostly intrinsic. For example, the higher ratio in Australia cannot be explained as due to background variations because GBM tends to have higher background over Australia than over the Americas (see appendix section A2). AGILE and Fermi have very different orbits and observe different areas. The inclination of the orbit of Fermi is 25.6°, while that of AGILE is only 2.5°, causing AGILE to observe a narrow band about the equator. AGILE cannot observe Australia, where GBM finds the highest TGF / lightning ratio. Despite the different areas observed, the geographic ratios found by the two instruments are very similar. For Fermi, the regions Americas : Africa : Asia have TGF / lightning ratios that compare as 1.00 : 0.47 : 0.55 (Table 3), while for AGILE the regions central

America : Africa : south-east Asia have ratios that compare as 1.0 : 0.40 : 0.50 [*Fuschino et al.*, 2011]. RHESSI has an orbit of 38° inclination and so observes more of the Earth than Fermi. A map comparing LIS/OTD lightning to RHESSI TGFs has qualitatively similar features: there is a deficit in Africa and excesses in central America, south-east Asia and Australia [*Smith et al.*, 2010]. This was interpreted as deficits inland and excesses in costal regions [*Hazelton*, 2009; *Smith et al.*, 2010]. This interpretation is consistent with the GBM observations; the Australia region has the highest TGF / lightning ratio (Table 3), which might be because it consists purely of coastal TGFs, while, for example, the Americas region is a mixture of coastal TGFs and oceanic TGFs from storms of the Intertropical Convergence Zone.

4.2. TEB / TGF Ratio

The high value obtained for the TEB / TGF ratio in the early GBM detections has been noted [*Fishman et al.*, 2011; *Carlson et al.*, 2011], but, the high value of this ratio in the earliest GBM results was very likely due to instrumental effects and the ratio has twice decreased, first with the improvement in the flight software trigger algorithms [*Fishman et al.*, 2011], then with use of the offline search. No detection method has been removed so the decreases in the ratio are the results of improvements in the detection of TGFs relative to TEBs. With the initial flight software algorithms that only used data from the NaI detectors, GBM detected only the most intense events: 2 TEBs and 13 TGFs in 487 days. During the next two years, following the improvement of the flight software to use the data of the BGO detectors, GBM triggered on 4 TEBs and 181 TGFs. The TGF rate changed from 9.8 per year to 90.0 per year, a large increase, while the TEB rate changed from 1.5 per year to 2.0 per year, consistent with no change.

Reasons for the increased detection rate include the higher energy range and higher effective area at higher energies of the BGO detectors, which increase the sensitivity for TGFs more than for TEBs owing to the harder energy spectra of the former. These factors do not fully explain the extreme relative change in the detection rates. 10% to 40% of the NaI counts for TGFs are in the overflow channel – those counts receive a larger deadtime, 10.4 μs instead of 2.6 μs, and consequently the number of counts detected by an NaI detector for sub-ms TGFs is greatly reduced, reducing the detection sensitivity for the original trigger algorithms that used only the data of the NaI detectors. Because the counts of TEBs are spread out over several to many ms these transients are less effected by deadtime and the detection sensitivity is little reduced in the NaI-only trigger algorithms. The first reduction in the observed GBM TEB / TGF ratio is evidence that an additional reason that augmenting the GBM flight software to trigger using BGO data lowered the GBM TGF detection threshold is the lower deadtime of the BGO detectors, which typically have zero or one overflow counts per TGF.

Observing to an even lower threshold using the offline search, 423 TGFs were detected and only two TEBs. The offline search increased the number of TGFs ten times but did not find any TEBs not already detected by on-board triggering. The improvement in sensitivity from the offline search is due to shortening the search windows. Shorter bin widths than the 16 ms accumulation used by the flight software are very useful for finding TGFs, which typically have durations $\lesssim$ 0.4 ms. Conversely, there is less difference between the durations of TEBs and the 16 ms flight accumulations and thus less sensitivity improvement by shortening the search window.

The main reason for not finding more TEBs is that shortening the search window is a small improvement for TEBs. We check whether some TEBs are not being found with the current offline search criteria because some TEBs produce signals predominantly on one side of Fermi, which might cause a problem with sample membership requirements 1 or 3 (section 2.2). Examining nine triggered TEBs we find that they range from the weakest, that would just barely be rejected by the offline search criteria (one $P_{\rm BGO} = 1.2 \times 10^{-3}$, versus requirement 1), to the strongest, that could be reduced by a factor of $\times$24 and still satisfy requirement 3 (number of BGO counts). One has a strong asymmetry between the two BGO detectors (count ratio 7.8) and three more have small asymmetries (ratios 1.6 to 1.9); the remaining four are fairly symmetrical (1.0 to 1.3) This suggests that adapting the offline search to accept signals predominantly on one side of Fermi probably would not gain many more TEBs. The limiting factor for GBM in detecting TEBs is the counts they produce in the GBM detectors, with the in-flight trigger algorithms already detecting most TEBs that are statistically significant above the background.

4.3. TGF Samples and Detection Methods

There are many reasons for differences in different TGF samples and their characteristics (e.g., fluence and duration thresholds), including differences both in the instruments and the methods for detecting TGFs. Important instrumental factors include differences in the dependence of the effective area with energy and especially differing deadtimes. In-orbit detection methods tend to be less flexible and limited to what is for TGFs relatively coarse time resolution. AGILE has the shortest in-orbit trigger timescale, at 293 μs [*Marisaldi et al.*, 2010a]. Ground-based offline search

algorithms are more flexible, at least when individual count data are available, allowing analysis at very high time resolution.

So far there have been three offline searches of individual count data, two of the RHESSI data [*Grefenstette et al.*, 2009; *Gjesteland et al.*, 2012] and that of this paper. All of the searches use multiple criteria, some of which we briefly summarize here. All three algorithms find the background rate from the data and the significance of candidates based upon the background rate. All of the searches had inter-detector comparisons and other tests to remove cosmic rays. Both RHESSI searches start with 1 ms windows. The first RHESSI search identified candidates as $\geq 12\sigma$ excesses in 1 ms bins [*Grefenstette et al.*, 2009], the second calculates the cumulative Poisson probability [*Gjesteland et al.*, 2012]. The GBM search uses many timescales, from 25 μs to 16 ms, and calculates cumulative Poisson probabilities, both of three time series and of their joint signal. The first RHESSI search identified runs as groups of counts without gaps exceeding 286 μs. Short runs (≤ 95 μs) were eliminated as likely cosmic rays [*Grefenstette et al.*, 2009]. The second search further analyzes events found on the 1 ms timescale by calculating Poisson probabilities on sliding windows on timescales of 0.3, 1 and 3 ms. Only events with durations between 0.1 and 3 ms were retained. Again, the short cut is used to remove cosmic rays [*Gjesteland et al.*, 2012]. The GBM search has no duration filter.

Important features of the GBM offline TGF search include requiring simultaneous, independent detections in multiple detectors, comparing the data between detectors to reject cosmic rays, using the data from the LAT calorimeter to reject cosmic rays, and searching on a wide range of timescales, from extremely short to longer than TGFs.

4.4. Cosmic Ray Background

The offline search found a large number of statistically significant excesses that were identified as cosmic ray showers, either automatically by their characteristics in the GBM data or by checking for high energy depositions in the LAT calorimeter. This points to cosmic ray showers as an important background for TGF observations. That cosmic rays could mimic TGFs was already known: both the original and revised RHESSI TGF criteria omit runs of counts shorter than 100 μs in order to exclude cosmic ray showers [*Grefenstette et al.*, 2009; *Gjesteland et al.*, 2012]. During the first year of GBM observations there were two triggers caused by cosmic rays that had some similarities to TGFs [*Briggs et al.*, 2010].

If the interaction of cosmic ray primaries with Fermi simply produced showers of secondaries with durations of microseconds, then the GBM detectors could not record enough counts to form a statistically significant signal because of their 2.6 μs deadtime per count (10.4 μs for the overflow channel). The events that are detected have durations similar to TGFs, from tens of μs to several ms. What process or processes produce counts on longer timescales? Long (ms) signals in individual NaI detectors can be caused by the passage of an energetic cosmic ray through that detector, which produces long-lived phosphorescence light emission [*Fishman and Austin*, 1977]. If a very energetic cosmic ray produced secondaries that reached numerous GBM detectors and which were themselves energetic enough to induce phosphorescence, then events that were long in multiple detectors, and therefore detectable, could be produced. However, phosphorescence events have soft spectra and BGO has much less phosphorescence light output than NaI [*Knoll*, 2000], while hard spectra and counts in the BGOs are observed

for the cosmic ray events. *Ulmer* [1994] suggested that energetic cosmic rays grazing the Earth's atmosphere produce gamma-ray showers of a few ms duration at satellites in low Earth orbit. *Briggs et al.* [2010] hypothesized that the energetic secondaries could induce radioactivity with up to ms timescale lifetimes. Perhaps both mechanisms take place.

This GBM TGF sample simultaneously has a low threshold and a high reliability of containing only TGFs due to the use of the LAT calorimeter data to remove cosmic ray events. Without the LAT data we would have had to 1) increase the threshold, 2) remove short events or 3) tolerate contamination. Excluding short events to avoid cosmic rays would further bias the TGF duration distribution beyond the limitations imposed by deadtime. Cosmic ray showers may be an unrecognized contamination in some TGF samples.

AGILE measurements show an additional spectral component extending to 100 MeV that is inconsistent with the standard predictions of the RREA processes [*Tavani et al.*, 2011]. *Celestin et al.* [2012] propose that non-equilibrium acceleration in the inhomogeneous fields of lightning leader tips with extremely high electric fields can produce the AGILE spectrum. Preliminary results place the AGILE high-energy emission into a 10% sub-population of TGFs that appears to have more uniform longitude and diurnal distributions than normally observed for TGFs [*Marisaldi et al.*, 2012a, b]. A cosmic ray contamination of the sub-population of AGILE TGFs responsible for the 100 MeV emission might explain the unexpected observations. Cosmic rays would have uniform longitude and diurnal distributions. Some cosmic rays that appear very similar to TGFs are clearly identified by GBM as events beginning with their highest energy count [*Briggs et al.*, 2010], which differs from three example

AGILE time histories [*Tavani et al.*, 2011]. Other cosmic rays not displaying this pattern are identified by their high-energy signature in the LAT calorimeter.

5. Summary

The new GBM TTE data mode and offline TGF detection method are detecting TGFs at a higher rate than ever before achieved. The improvement in the detection rate over the previous on-board GBM detection method is approximately ten-fold. Even though the threshold has been lowered, the sample reliably contains only TGFs by use of the LAT calorimeter data to remove cosmic ray showers – the residual contamination is estimated at $\sim$2%. The sample was tested by observing control regions where TGFs are not expected. False positives would have appeared in the TGF-active and control regions at a rate approximately proportional to the observing time. Only one event passed the criteria in the control regions, for a detection rate more than $\times$70 lower than the detection rate in the TGF-active regions. Another verification was comparing the association rate with WWLLN locations of the new sample to the rate found for GBM triggered TGFs. With GBM triggered TGFs the association rate with WWLLN locations is 27.6%, while the association rate for the weaker and shorter (on average) TGFs found with the offline search of the continuous TTE data is higher (35%), which limits how many non-TGFs could be in the sample. The difference between the association rates is further discussed by *Connaughton et al.* [2012].

The new sample of TGFs found in the GBM TTE data shows that the durations of TGFs extend to shorter values than previously found (Fig. 10). The intrinsic duration distribution likely contains more TGFs shorter than $\lesssim 50$ μs than are being detected because GBM has higher deadtime fractions for these events. The consistently high

deadtime fractions for the shortest events (Figure 11) means that the observed counts need greater correction to obtain the true intensities. The relativistic feedback discharge model of *Dwyer* [2012] predicts that for a given electric field configuration shorter TGFs often produce more runaway electrons than longer ones. This implies even higher gamma-ray fluxes in the shorter duration, which may be difficult to detect and measure with current TGF instruments.

The sample is large enough and the WWLLN detection efficiency is high enough that there are now a large number of TGFs with associated WWLLN locations and thus source locations to ≈10 km accuracy. Maps of these VLF geolocations reveal the geographic and meteorological patterns of the sources more clearly than maps of the spacecraft locations (Fig. 6).

The distribution of offsets between the spacecraft nadirs and the source locations is wider than previously observed with GBM (Fig. 8). Triggered GBM TGFs have offsets extending to 300 km, while offsets of the less intense TGFs of this sample extend to ∼800 km. The distribution is consistent with a uniform TGF detection efficiency to ≈300 km, beyond which it quickly falls.

To compensate for the selective collection of the GBM data we normalized the GBM TGF rates to the lightning rates of LIS/OTD. The calculation uses the measured detection efficiency of GBM as a function of offset from the nadir to determine what fraction of TGFs are observed, and thus how many TGFs exist compared to the total amount of lightning. We find a ratio of $f_{\mathrm{T/L}} \approx \frac{1}{2600}$ between TGFs above GBM's threshold and LIS/OTD lightning flashes. As previously found, this ratio varies geographically. Multiplying the TGF / lightning ratio by the LIS/OTD lightning rate,

by region, we estimate the rate of TGFs above GBM's intensity threshold as ≈400,000 per year between latitudes ±25.6°.

The continuous TTE data mode was extended from selected regions to production for the entire orbit outside of the SAA on 26 November 2012; we estimate that with these data GBM will detect about 850 TGFs per year. The increased sample size and improved exposure uniformity will increase the usefulness of Fermi for studies of TGF properties and TGF-meteorological correlations. The comprehensive coverage will uncover more TGFs in unusual locations, such as the TGF deep in the Atlantic that was fortuitously found in GRB TTE data (Figure 14). We will investigate improved rejection of the cosmic ray background and also selection criteria to accept TGFs that have a strong signal on one side of the spacecraft and a weak signal on the other. The complete continuous TTE coverage will enhance the astrophysics capabilities of GBM. Additional characteristics of this GBM TGF sample, including new interpretations of radio observations of TGFs, are reported by *Connaughton et al.* [2012].

Appendix A: Details of Search and Sample Criteria

A1. Initial Sample

This Appendix further describes the search method, the TGF selection criteria and the reasons for those criteria. As part of that analysis it uses an initial TGF candidate sample based on relaxed criteria. Because of the relaxed criteria, this initial sample contains more candidates than the reliable sample of the main text. The search was initially done with a threshold of $P_{\rm joint}^{\rm corr} \leq 1 \times 10^{-8}$ (modification of requirement 4) and without applying the LAT cosmic ray filter (requirement 7). With these two modifications, the offline search applied to the 1217.7 hours of continuous TTE from

both the TGF-active and control regions (Table 1) results in an initial sample of 632 TGF/TEB candidates (Fig. 15). The 7.1 hours of TTE generated by TGF triggers are omitted so that the intense triggered TGFs are not included in the initial sample. There are 598 candidates in the 1029.6 hours of continuous TTE data from the the TGF-active regions in which TGFs are likely (i.e., the Americas, Africa, Australia and Asia regions) and 34 candidates from 188.1 hours of continuous TTE collected from the three control regions, including seven in North Africa. Tables 4 and 5 list properties of the sample for the TGF active and control regions, including as a function of $P_{\rm joint}^{\rm corr}$.

A2. Binning for the Search

For each "pass" of Fermi through one of the regions, the TTE data are binned at sixteen different bins widths (Table 2). For each bin width the data are summed at four phases, at offsets of 0, 0.25 0.5 and 0.75 of the width of the bin. Binning at multiple phases avoids the problem of a TGF straddling a bin boundary, causing its signal to be divided between two bins and becoming statistically insignificant.

The data of both detector types are recorded in 128 pseudo-logarithmic channels. While the two detector types both use 128 channels, the energy boundaries are different. For both detector types, the highest channel, channel 127, is an integral, or overflow channel, that includes all counts from the starting energy of the channel to infinity. Occasionally overflow counts also appear in channel 126 and less commonly in channel 125. TGFs and TEBs rarely cause counts in the BGO overflow channels, while high-energy cosmic rays often produce counts in those channels. Channels 1 and 2 are below the data collection threshold. Therefore to optimize the signal-to-background ratio the search is based on BGO channels 3 to 125, corresponding to ≈300 keV to ≈40

MeV. Since many TGF and TEB counts in the NaI detectors are above 1 MeV, the starting energy of the overflow channel, that channel has useful signal. Initially the search summed all NaI channels. Starting on 31 March 2011 the summation of the NaI data was limited to energy channels 22 to 127, corresponding to $\gtrsim$30 keV, to avoid intermittent very high background rates below $\approx$ 25 keV from increased solar activity. (This implies that "discovery counts" changed slightly in meaning on this date due to the change in the the NaI channel range summed into discovery counts.) In the BGO detectors the background is typically $\sim$ 1.5 counts per ms, while for the updated NaI channel selection the typical background rate, summed over the 12 NaI detectors, is $\sim$ 8 counts per ms. Particle fluxes in the SAA, primarily protons, induce radioactivity so that passes over Africa that emerged from the SAA can have much higher background rates. The BGO rates can be as high as $\sim$ 6 counts per ms when entering the Africa region; the summed NaI rate as high as $\sim$ 25 counts per ms. The elevated rates decline rapidly in the Africa region and more slowly past Africa.

A3. GBM Cosmic Ray Criteria

The cosmic ray showers that cause on-board triggers are so intense that they are simultaneously (within the 2 μs timing resolution of GBM) detected by most of the GBM detectors; the offline search detects some showers that have most of their signal on one side of the spacecraft. These weaker one-sided cosmic rays are identified by the following characteristics occurring simultaneously within the 2 μs timing resolution of GBM in the detectors on one side of Fermi: 1) an overflow count in the BGO detector, 2) counts in at least five of the six NaI detectors on that side, and 3) at least four of those NaI counts being in the overflow channel. These criteria were designed to be as

narrow as possible so as to make the probability of removing a TGF extremely low. These criteria also identify the more intense cosmic ray showers that are visible on both sides of the spacecraft. Cosmic ray events identified by these criteria are automatically removed and are not included in any sample described in this paper (requirement 6).

A4. LAT Cosmic Ray Test

The LAT calorimeter data are examined to remove cosmic ray showers that were not removed by the automatic GBM filter. Candidate TGFs that contain LAT events with total energy depositions in the calorimeter > 10 GeV are removed from the sample (requirement 7, section 2.3.2). Cosmic ray showers that deposit > 10 GeV are detected in the LAT with high efficiency, but not all such showers are telemetered to the ground. About 10% will be missed because they arrive during dead time from a preceding particle or gamma ray. Others will be missed because they are rejected by the LAT on-board filter, which reduces the number of cosmic rays in the LAT data stream. Details of the on-board LAT event detection and filtering can be found in *Atwood et al.* [2009].

The on-board filter handles events above and below 20 GeV differently. Specifically, the filter retains and sends to the ground all events that deposit > 20 GeV in the calorimeter. Thus all showers above 20 GeV that do not arrive during dead time will be present in the LAT data stream for use in our cosmic ray test. Below 20 GeV, the on-board filter rejects hadronic showers with good efficiency so that these events are typically not sent to the ground. Some cosmic ray showers masquerading as TGFs in GBM deposit 10–20 GeV in the calorimeter and are therefore subject to removal by the filter, which reduces the effectiveness of the cosmic ray test. This energy range is useful nonetheless: if we had increased the energy threshold of the cosmic ray test to 20 GeV

the number of cosmic ray shower identifications would have been reduced from 182 to 173, allowing 9 cosmic ray showers to leak into the TGF sample.

We can set a limit on the fraction of unidentified cosmic ray showers leaking through the LAT test for any reason. In the control regions this test identified 85% of the candidate TGFs as cosmic rays (Table 5). If we assume that all control region candidates are cosmic ray showers, then an estimate of the rate of failing to identify cosmic ray showers as such is 15%.

A5. Sample Quality

We can determine the association rate between the candidates of a sample and WWLLN observations and test whether the sample consist solely of TGFs. Comparing the association rate of samples found in the continuous TTE with the offline search with the association rate of triggered TGFs, we can infer that a sample contains false positives if its match rate is appreciably lower. (By only comparing samples found in the continuous TTE to the reference sample of triggered TGFs the two samples are always independent.) The true GBM / WWLLN association rate is not known; we only have observed a finite sample of triggered TGFs to estimate it. Therefore the testing of the plausibility of the association rate of a sample is done as the comparison of the rates observed in two samples: that sample and the reference sample of triggered TGFs. We find the association rate for which the two samples are most consistent and use that best common association rate to find the consistency probability as the probability of the sample with the higher rate having its observed association rate or higher times the probability of the sample with the lower rate having its observed association rate or lower [*Smith et al.*, 1996]. There may be reasons other than sample contamination for

two samples to have different association rates: 1) the TGF / WWLLN association rate depends on TGF duration [*Connaughton et al.*, 2012], which might differ on average between the two samples, 2) the detection efficiency of WWLLN varies geographically [*Rodger et al.*, 2009], 3) as does the TGF / lightning ratio [*Smith et al.*, 2010; *Fuschino et al.*, 2011] (also Table 3). 4) It is possible that weaker TGFs have lower association rates. Despite these caveats, finding that a sample has an association rate much lower than the expected rate is highly suggestive that the sample contains non-TGFs.

The first comparisons of triggered GBM TGFs and WWLLN observations found an association rate of 33% [*Briggs et al.*, 2010; *Connaughton et al.*, 2010], which is much higher than the overall WWLLN detection efficiency for lightning and very similar to the WWLLN detection efficiency for very high current lightning [*Abarca et al.*, 2010]. A GBM TGF and a WWLLN location are considered associated if the WWLLN location is within 1000 km of the nadir of Fermi and is within ±10 ms of the TGF [*Connaughton et al.*, 2012]. Extending the sample, GBM triggered on 174 TGFs from the enabling of the trigger on 11 July 2008 to 31 August 2011, of which 48 have an associated WWLLN location, for an association rate of 27.6%.

The candidates of the control sample have no WWLLN associations and the maps of discharges within ±600 s of the candidate times show only a few discharges for the entire sample within 1000 km of candidates. For GBM triggered TGFs, even when associations with specific WWLLN locations were not found, clusters of WWLLN detected lightning locations indicating storms were almost always found within 300 km of the nadir. Out of 50 TGFs, only one in Africa, where WWLLN had lower detection efficiency, lacked WWLLN lightning clusters [*Connaughton et al.*, 2010]. The paucity of

lightning for the candidates in the control regions makes it likely that very few or none are TGFs. The detection efficiency of WWLLN in the Southeast Pacific TTE region is high, comparable to WWLLN's detection efficiency in the Americas region. The WWLLN detection efficiency in the Indian Ocean and North Africa regions is lower, but ranges from similar to higher than the detection efficiency in the Africa regions [*Hutchins et al.*, 2012]. The almost complete lack of lightning discharges near candidates in the control regions cannot be attributed to geographic variations in the detection efficiency of WWLLN. The lack of lightning is consistent with the identification using LAT data of 85% of these control-region candidates as cosmic ray showers.

Two candidates in the control regions were most significant for long bins (>= 2 ms) and therefore might be TEBs, which are longer than TGFs. Since for TEBs the source is at the end of the magnetic field line through Fermi, far from the nadir of Fermi, those footprint locations are also checked for lightning activity. There are no WWWLN-detected lightning locations within 200 km of any of the magnetic footprints of the two candidates. One is identified by the LAT as a cosmic ray shower. These two events are unlikely to be TEBs.

The sample of 598 candidates in the TGF-active regions has a WWLLN-match rate of 24%. All of these candidates are short (i.e., most significant bin width is 1.4 ms or shorter) so they are unlikely to be TEBs and therefore only the areas under Fermi are examined in the WWLLN data. This sample is most consistent with the 174 triggered TGFs at a common association rate of 23.8%, for a consistency probability with a common rate of 6.6%. While the entire TGF-active region offline search sample and the triggered TGFs are consistent with a common association rate, some sub-samples are

not. For example, the sub-sample of low significance candidates ($P_{\rm joint}^{\rm corr} = 10^{-11}$ to 10^{-8}) has a very low TGF / WWLLN association rate, only 3% (Table 4). The common rate that achieves the best consistency between this sample and the 174 triggered TGFs is 15.3%, for a probability that the two samples have a common association rate of only $\sim 10^{-12}$.

Evidence that the initial sample is contaminated with non-TGFs, with a higher false-positive rate in the control regions and a higher false-positive rate for lower significance candidates (higher $P_{\rm joint}^{\rm corr}$) (see Tables 4 and 5), includes:

1. due to the rarity of lightning in the control regions and prior TGF observations, we expect very few or no TGFs in the control regions, but candidates are found using the initial criteria,

2. high-energy depositions in the LAT calorimeter identify some of the candidates as cosmic ray showers, with a very high fraction (85%) in the control regions and higher fractions for lower significance candidates of the TGF-active regions,

3. the WWLLN association rate is lower than the association rate of GBM triggered TGFs, especially in the control regions and for the low-significance candidates of the TGF-active regions,

4. the candidates in the control boxes are skewed to lower significances compared to those of the TGF-active regions.

A6. Final Criteria

A reliable TGF sample is created from the initial sample of 632 events found in the continuous TTE (section A1) by adjusting the criteria based on the analysis of the the GBM / WWLLN association rates and the identification of cosmic ray events with the

LAT calorimeter data. First the threshold for $P_{\rm joint}^{\rm corr}$ is set to 1×10^{-11} (requirement 4). With the very high cosmic ray rate between $P_{\rm joint}^{\rm corr}$ of 10^{-11} to 10^{-8} (67%) and the incomplete rejection of cosmic rays by the LAT test (section A4), the number of residual cosmic ray events would be unacceptable if we tried to retain this group and so it is best to eliminate this highly contaminated group. This removes 76% (116) of the 153 candidates identified as cosmic ray showers using the LAT calorimeter.

Of the remaining 421 candidates in the TGF-active regions (i.e., those with $P_{\rm joint}^{\rm corr} \leq 10^{-11}$) only 9% (37) are identified as cosmic ray showers by having a high-energy deposition in the LAT calorimeter. These cosmic ray showers are removed from the sample (requirement 7 – see section 2.3.2).

With the threshold $P_{\rm joint}^{\rm corr} = 1 \times 10^{-11}$ and the removal of all LAT identified cosmic ray showers, 33 of the 34 initial sample candidates in the control regions are removed, showing the effectiveness of the criteria. We do not use the remaining control region event as a TGF. Applying the final criteria (section 2.2) to the 598 initial sample candidates in the TGF-active regions creates a sample of 384 new TGFs found in the continuous TTE resulting in the sample described in section 2.4.

We retain the seven candidates in the sub-sample defined by $P_{\rm joint}^{\rm corr} \leq 10^{-11}$ for which LAT data are not available since, based on the 9% cosmic ray rate for the events of this sample with LAT data, only ≈ 0.6 of these candidates is expected to be a cosmic ray shower. Based on the ≈15% deadtime (section A4) of the LAT cosmic ray test and the 37 LAT-detected cosmic ray showers in the sample, there are probably an additional ≈6.5 cosmic ray showers that were missed. The two leakages indicate a contamination of ≈ 7 cosmic ray showers, or ∼2% of this sample.

Thirty-three (97%) candidates in the control regions and 214 (36%) in the TGF-active regions are removed from the initial sample. These values are 0.18 ± 0.03 and 0.21 ± 0.01 per hour, respectively, which are consistent with the same rates of removal and causes of falses positives in the two types of regions. Assuming that the candidates in the control region are all non-TGFs (at least 85% are cosmic rays), the consistent removal rates suggests that few TGFs have been removed from the final sample in the TGF-active regions.

Three candidates with WWLLN associations, out of a total of 141 candidates with WWLLN associations found in the continuous TTE with the offline search, are identified as cosmic ray events by having a high-energy deposition in the LAT calorimeter and are therefore not included in the sample of 384 TGFs despite likely associations with lightning signals. (Eight triggered TGFs and one triggered TEB have WWLLN associations – none of these are identified as cosmic ray events by the LAT.) Some GBM TGF / WWLLN associations might be false positives, as might be the identifications as a cosmic rays. We examine the arrival times of the GBM counts to determine the nature of these events. One of the candidates starts with counts from many detectors simultaneously to the 2 μs resolution of GBM. While the counts do not meet the GBM criteria for a cosmic ray (the BGO count is not in the overflow channel) (see section A3), the count pattern in the GBM data supports the cosmic ray identification and indicates that this candidate was correctly removed from the TGF sample. Another candidate has a large number of simultaneous counts, followed by a time gap, then counts that appear to belong to a TGF. This candidate is probably a cosmic ray followed by a TGF; the LAT detection of the high-energy deposition in the calorimeter from the cosmic ray

causes the loss of a genuine TGF from the sample. The nature of the last is uncertain. Using two as the maximum number of TGFs misidentified as cosmic rays gives an upper-limit to the mistaken removal rate of TGFs from the sample due to the LAT calorimeter criterion (requirement 7) of 1.3%.

Appendix B: Earlier Samples

B1. Earlier GBM Sample

Østgaard et al. [2012] analyzed the intensity distribution of TGFs using the observations of RHESSI, GBM and ADELE, including preliminary results of the GBM offline search based upon a talk [*Briggs*, 2011] and confirming private communications. At the time of the talk in July 2011 only 591.8 hours of continuous TTE through 30 March 2011 had been searched, resulting in 234 new TGFs with the criteria then in use. During the same regions and time period there were 23 triggered TGFs, for a ratio between the methods of $234/23 = 10.2 \pm 2.2$ and a TGF detection rate increase of $(234 + 23)/23 = 11.2 \pm 2.4$. The comparable values for the final sample are $384/41 = 9.4 \pm 1.5$ as the ratio of the methods and $(384 + 41)/41 = 10.4 \pm 1.7$ as the detection rate increase. The agreement between the values for the two samples is unsurprising since the TTE data of the preliminary sample is a subset (57%) of the final data. Besides statistical fluctuations between the overlapping samples, the values might differ due to systematics: the selection criteria have changed since the summer of 2011, with improvements in the selection of TGFs and in the removal of cosmic rays. Using the current search criteria (section 2.2) applied to the continuous TTE up to 30 March 2011, 17 former TGFs are reclassified as cosmic rays and 10 events are added as TGFs so that the number of TGFs becomes 227. (There is no change to the triggered TGFs.) While

this number is fully consistent with 57% of the total sample (i.e., $0.57 \times 384 = 218.9$), agreement is not required since the TTE data collection regions varied with time, and the two samples have different mixtures of regions and times of the year.

B2. RHESSI samples

Section 3.4.1 derives the TGF detection rate expected for GBM with continuous collection of TTE, instead of the selective collection used for the sample of this paper, obtaining ≈850 TGFs per year. (Section 3.5 makes an independent estimate of ~ 500 TGFs per year.) Section 3.4.1 proceeds to compare to the RHESSI detection rate of the current most sensitive search of the RHESSI data, that of *Gjesteland et al.* [2012], obtaining $\times 1.5$ as the TGF detection rate difference between the instruments due to sensitivity differences. This is the most pertinent comparison of the relative detection rates of the instruments.

Section 3.2 compares the TGF observations of the two instruments as rate densities. Based on the availability of the RHESSI offset distribution data [*Collier et al.*, 2011], results from the original RHESSI search method [*Grefenstette et al.*, 2009] were used despite its lower detection rate. This comparison gave a TGF detection rate ratio between the instruments/searches due to their different sensitivities of $\times 3.5$. In this appendix we include some additional comparisons to the original RHESSI search method.

Collier et al. [2011] used 972 TGFs found using the original RHESSI criteria [*Grefenstette et al.*, 2009], for an average TGF detection rate of 0.31 TGFs per day. This sample has a lower average detection rate because it includes data after the RHESSI detectors suffered radiation damage [*Grefenstette et al.*, 2009]. Comparing to the

estimated GBM detection rate for continuous TTE collection of 2.3 TGFs per day, the ratio between detection rates is 7.3. Removing the portion of the rate difference due to the different latitude ranges (×1.65), the detection rate ratio due to sensitivity differences is ×4.4.

Using preliminary results of the GBM offline search (Appendix B1, see section 3.4.1), *Østgaard et al.* [2012] estimated the unbiased GBM detection rate. Combining this with a RHESSI sample of 591 TGFs found with the original search method [*Grefenstette et al.*, 2009], which had a detection rate of 0.42 TGFs per day, and the correction factor of 1.65 for the different TGF activities under the different orbits, they obtain a factor of 3.6 for the relative detection rates of the instruments due to sensitivity differences.

These various values for the relative detection rates of the instruments due to sensitivity differences are consistent if one considers the differences between the samples and the uncertainties.

Acknowledgments. We thank Richard Blakeslee, Garry Case, Martino Marisaldi, David Smith, Steven Cummer and Michael Splitt for discussions or assistance. The Fermi GBM Collaboration acknowledges support for GBM development, operations, and data analysis from National Aeronautics and Space Administration (NASA) in the United States and from the Bundesministerium für Wirtschaft und Technologie (BMWi) / Deutsches Zentrum für Luft und Raumfahrt (DLR) in Germany. This work was supported in part by the Fermi Guest Investigator Program. The authors wish to thank the World Wide Lightning Location Network (http://wwlln.net), a collaboration among over 50 universities and institutions, for providing the lightning location data used in this paper. The Fermi LAT Collaboration acknowledges generous ongoing support from

a number of agencies and institutes that have supported both the development and the operation of the LAT as well as scientific data analysis. These include NASA and the Department of Energy in the United States, the Commissariat ‘a lEnergie Atomique and the Centre National de la Recherche Scientifique / Institut National de Physique Nucleaire et de Physique des Particules in France, the Agenzia Spaziale Italiana and the Istituto Nazionale di Fisica Nucleare in Italy, the Ministry of Education, Culture, Sports, Science and Technology (MEXT), High Energy Accelerator Research Organization (KEK) and Japan Aerospace Exploration Agency (JAXA) in Japan, and the K. A. Wallenberg Foundation, the Swedish Research Council and the Swedish National Space Board in Sweden. G. F. acknowledges the support of the Irish Research Council for Science, Engineering and Technology. S. F. acknowledges the support of the Irish Research Council for Science, Engineering and Technology, cofunded by Marie Curie Actions under FP7. D. T. acknowledges support from Science Foundation Ireland under grant number 09-RFP-AST-2400. The authors thank Nikolai Ostgaard and an anonymous reviewer for their comments, which improved the paper.

References

Abarca, S. F., K. L. Corbosiero, and T. J. Galarneau, Jr (2010), An evaluation of the worldwide lightning location network (WWLLN) using the national lightning detection network (NLDN) as ground truth, *J. Geophys. Res.*, *115*, D18,206, doi:10.1029/2009JD013411.

Atwood, W. B., et al. (2009), The Large Area Telescope on the Fermi gamma-ray space telescope mission, *ApJ*, *697*, 1071, doi:10.1088/0004-637X/697/2/1071.

Boccippio, D. J., K. L. Cummins, H. J. Christian, and S. J. Goodman (2001), Combined satellite- and surface-based estimation of the intracloud–cloud-to-ground lightning ratio over the continental united states, *Mon. Wea. Rev.*, *129*, 108, doi:doi:10.1175/1520-0493(2001)129⟨0108:CSASBE⟩2.0.CO;2.

Boccippio, D. J., W. J. Koshak, and R. J. Blakeslee (2002), Performance assessment of the optical transient detector and lightning imaging sensor. part i: Predicted diurnal variability, *Journal of Atmospheric and Oceanic Technology*, *19*, 1318.

Briggs, M. S. (2011), More TGFs from GBM, http://www.uah.edu/cspar/conferences/163-cspar/2911-tgf-workshop, TGF Workshop 2011.

Briggs, M. S., et al. (2010), First results on terrestrial gamma-ray flashes from the Fermi gamma-ray burst monitor, *J. Geophys. Res.*, *115*, A07,323, doi:10.1029/2009JA015242.

Briggs, M. S., et al. (2011), Electron-positron beams from terrestrial lightning observed with Fermi GBM, *Geophys. Res. Lett.*, *38*, L02,808, doi:10.1029/2010GL046259.

Carlson, B. E., N. G. Lehtinen, and U. S. Inan (2009), Terrestrial gamma ray flash production by lightning current pulses, *J. Geophys. Res.*, *114*, A00E08, doi:10.1029/2009JA014531.

Carlson, B. E., N. G. Lehtinen, and U. S. Inan (2010), Terrestrial gamma ray flash production by active lightning leader channels, *J. Geophys. Res.*, *115*, A10,324, doi:10.1029/2010JA015647.

Carlson, B. E., T. Gjesteland, and N. Østgaard (2011), Terrestrial gamma-ray flash electron beam geometry, fluence, and detection frequency, *J. Geophys. Res.*, *116*, A11,217, doi:10.1029/2011JA016812.

Celestin, S., and V. P. Pasko (2011), Energy and fluxes of thermal runaway electrons produced by exponential growth of streamers during the stepping of lightning leaders and in transient luminous events, *J. Geophys. Res.*, *116*, A03,315, doi:10.1029/2010JA016260.

Celestin, S., W. Xu, and V. P. Pasko (2012), Terrestrial gamma-ray flashes with energies up to 100 MeV produced by non-equilibrium acceleration of electrons in lightning, *J. Geophys. Res.*, *117*, A05,315, doi:10.1029/2012JA017535.

Christian, H. J., et al. (2003), Global frequency and distribution of lightning as observed from space by the optical transient detector, *J. Geophys. Res.*, *108*, 4005, doi:10.1029/2002JD002347.

Collier, A. B., T. Gjesteland, and N. Østgaard (2011), Assessing the power law distribution of TGFs, *J. Geophys. Res.*, *116*, A10,320, doi:10.1029/2011JA016612.

Connaughton, V., et al. (2010), Associations between Fermi GBM terrestrial gamma-ray flashes and sferics from the WWLLN, *J. Geophys. Res.*, *115*, A12,307, doi:10.1029/2010JA015681.

Connaughton, V., et al. (2012), Radio signals from electron beams in terrestrial gamma-ray flashes, *J. Geophys. Res.*, doi:10.1029/2012JA018288, in press.

Cummer, S. A., G. Lu, M. S. Briggs, V. Connaughton, S. Xiong, G. J. Fishman, and J. R. Dwyer (2011), The lightning-TGF relationship on microsecond timescales, *Geophys. Res. Lett.*, *38*, L14,810, doi:10.1029/2011GL048099.

Dowden, R. L., J. B. Brundell, and C. J. Rodger (2002), VLF lightning location by time of group arrival (TOGA) at multiple sites, *Journal of Atmospheric and Solar-Terrestrial Physics*, *64*, 817–830, doi:10.1016/S1364-6826(02)00085-8.

Dwyer, J. R. (2003), A fundamental limit on electric fields in air, *Geophys. Res. Lett.*, *30*, ASC8.1–ASC8.4, doi:10.1029/2003GL017781.

Dwyer, J. R. (2008), Source mechanisms of terrestrial gamma-ray flashes, *J. Geophys. Res.*, *113*, D10,103, doi:10.1029/2007JD009248.

Dwyer, J. R. (2012), The relativistic feedback discharge model of terrestrial gamma ray flashes, *J. Geophys. Res.*, *117*, A02,308, doi:10.1029/2011JA017160.

Dwyer, J. R., et al. (2004), A ground level gamma-ray burst observed in association with rocket-triggered lightning, *Geophys. Res. Lett.*, *31*, L05,119, doi:10.1029/2003GL018771.

Dwyer, J. R., B. W. Grefenstette, and D. M. Smith (2008), High-energy electron beams launched into space by thunderstorms, *Geophys. Res. Lett.*, *35*, L02,815, doi:10.1029/2007GL032430.

Dwyer, J. R., D. M. Smith, and S. A. Cummer (2012a), High-energy atmospheric physics: Terrestrial gamma-ray flashes and related phenomena, *Space Science Reviews*, *173*, 133–196, doi:10.1007/s11214-012-9894-0.

Dwyer, J. R., M. M. Schaal, E. Cramer, S. Arabshahi, N. Liu, H. K. Rassoul, J. D. Hill, D. M. Jordan, and M. A. Uman (2012b), Observation of a gamma-ray flash at ground level in association with a cloud-to-ground lightning return stroke, *J. Geophys. Res.*, *117*, A10,303, doi:10.1029/2012JA017810.

Fishman, G., and R. Austin (1977), Large-area multi-crystal NaI(Tl) detectors for x-ray and gamma-ray astronomy, *Nucl. Instrum. Methods*, *140*, 193–196, doi:10.1016/0029-554X(77)90085-4.

Fishman, G. J., et al. (1994), Discovery of intense gamma-ray flashes of atmospheric origin, *Science*, *264*, 1313–1316.

Fishman, G. J., et al. (2011), Temporal properties of terrestrial gamma-ray flashes from the gamma-ray burst monitor on the Fermi observatory, *J. Geophys. Res.*, *116*, A07,304, doi:10.1029/2010JA016084.

Fuschino, F., et al. (2011), High spatial resolution correlation of AGILE TGFs and global lightning activity above the equatorial belt, *Geophys. Res. Lett.*, *38*, L14,806, doi:10.1029/2011GL047817.

Gjesteland, T., N. Østgaard, P. H. Connell, J. Stadsnes, and G. J. Fishman (2010), Effects of dead time losses on terrestrial gamma ray flash measurements with the Burst and Transient Source Experiment, *J. Geophys. Res.*, *115*, A00E21, doi:10.1029/2009JA014578.

Gjesteland, T., N. Østgaard, A. B. Collier, B. E. Carlson, M. B. Cohen, and N. G. Lehtinen (2011), Confining the angular distribution of terrestrial gamma ray flash emission, *J. Geophys. Res.*, *116*, A11,313, doi:10.1029/2011JA016716.

Gjesteland, T., N. Østgaard, A. B. Collier, B. E. Carlson1, C. Eyles, and D. M. Smith (2012), A new method reveals more TGFs in the RHESSI data, *Geophys. Res. Lett.*, *39*, L05,102, doi:10.1029/2012GL050899.

Grefenstette, B. W., D. M. Smith, J. R. Dwyer, and G. J. Fishman (2008), Time evolution of terrestrial gamma ray flashes, *Geophys. Res. Lett.*, *35*, L06,802, doi:10.1029/2007GL032922.

Grefenstette, B. W., D. M. Smith, B. J. Hazelton, and L. I. Lopez (2009), First RHESSI terrestrial gamma ray flash catalog, *J. Geophys. Res.*, *114*, A02,314,

doi:10.1029/2008JA013721.

Gurevich, A. V., G. M. Milikh, and R. Roussel-Dupre (1992), Runaway electron mechanism of air breakdown and preconditioning during a thunderstorm, *Physics Letters A*, *165*, 463–468.

Hazelton, B. J., B. W. Grefenstette, D. M. Smith, J. R. Dwyer, X.-M. Shao, S. A. Cummer, T. Chronis, E. H. Lay, and R. H. Holzworth (2009), Spectral dependence of terrestrial gamma-ray flashes on source distance, *Geophys. Res. Lett.*, *36*, L01,108, doi:10.1029/2008GL035906.

Hazelton, B. J. C. (2009), Statistical studies and modeling of RHESSI terrestrial gamma-ray flashes, Ph.D. thesis, University of California Santa Cruz.

Hutchins, M. L., R. H. Holzworth, J. B. Brundell, and C. J. Rodger (2012), Relative detection efficiency of the world wide lightning location network, *Radio Sci*, *47*, RS6005, doi:10.1029/2012RS005049.

Knoll, G. F. (2000), *Radiation Detection and Measurement*, third ed., John Wiley, New York.

Lu, G., et al. (2010), Lightning mapping observation of a terrestrial gamma-ray flash, *Geophys. Res. Lett.*, *37*, L11,806, doi:10.1029/2010GL043494.

Mach, D. M., H. J. Christian, R. J. Blakeslee, D. J. Boccippio, S. J. Goodman, and W. L. Boeck (2007), Performance assessment of the optical transient detector and lightning imaging sensor, *J. Geophys. Res.*, *112*, D09,210, doi:10.1029/2006JD007787.

Marisaldi, M., F. Fuschino, C. Labanti, M. Galli, F. Long, E. D. Monte, et al. (2010a), Detection of terrestrial gamma-ray flashes up to 40 MeV by the AGILE satellite, *J. Geophys. Res.*, *115*, A00E13, doi:10.1029/2009JA014502.

Marisaldi, M., A. Argan, A. Trois, A. Giuliani, M. Tavani, C. Labanti, F. Fuschino, et al. (2010b), Gamma-ray localization of terrestrial gamma-ray flashes, *Phys. Rev. Lett*, *105*, 128,501, doi:10.1103/PhysRevLett.105.128501.

Marisaldi, M., et al. (2011), AGILE observations of terrestrial gamma-ray flashes, *http://arxiv.org/abs/1111.2188v1*, eConf C110509.

Marisaldi, M., F. Fuschino, M. Tavani, C. Labanti, A. Argan, S. Dietrich, and M. Formenton (2012a), Two TGF populations detected by AGILE?, `http://www.asdc.asi.it/10thagilemeeting/dwl.php?file=workshop_files/6.Marisaldi_introduction.pdf`, AGILE 10th Science Workshop: Lightning, Terrestrial Gamma-Ray Flashes, and Meteorology.

Marisaldi, M., F. Fuschino, M. Tavani, C. Labanti, A. Argan, S. Dietrich, and M. Formenton (2012b), Two TGF populations detected by AGILE?, `http://www.asdc.asi.it/10thagilemeeting/dwl.php?file=workshop_files/6.Marisaldi_AGILE_10th_WS.pdf`, AGILE 10th Science Workshop: Lightning, Terrestrial Gamma-Ray Flashes, and Meteorology.

Marshall, T. C., and M. Stolzenburg (2001), Voltages inside and just above thunderstorms, *J. Geophys. Res.*, *106*, 4757–4768.

Meegan, C. A., et al. (2009), The Fermi gamma-ray burst monitor, *ApJ*, *702*, 791–804, doi:10.1088/0004-637X/702/1/791.

Nemiroff, R. J., J. T. Bonnell, and J. P. Norris (1997), Temporal and spectral characteristics of terrestrial gamma flashes, *J. Geophys. Res.*, *102*, 9659–9665.

Nikiforov, A. M. (1994), Exact Smirnov two-sample tests for arbitrary distributions, *Appl. Statist.*, *43*, 265–284.

Østgaard, N., T. Gjesteland, J. Stadsnes, P. H. Connell, and B. Carlson (2008), Production altitude and time delays of the terrestial gamma flashes: Revisiting the burst and transient source experiment spectra, *Journal of Geophys. Res.*, *113*, A02,307, doi:10.1029/2007JA012618.

Østgaard, N., Gjesteland, R. S. Hansen, A. B. Collier, and B. Carlson (2012), The true fluence distribution of terrestrial gamma flashes at satellite altitude, *J. Geophys. Res.*, *117*, A03,327, doi:10.1029/2011JA017365.

Paciesas, W. S., et al. (2012), The Fermi GBM gamma-ray burst catalog: the first two years, *ApJS*, *199*, 18, doi:10.1088/0067-0049/199/1/18.

Rodger, C. J., J. B. Brundell, R. H. Holzworth, and E. H. Lay (2009), Growing detection efficiency of the world wide lightning location network, in *Conf. Proc. 1118, Coupling of Thunderstorms and Lightning Discharges to Near-Earth Space*, edited by N. B. Crosby, T.-Y. Huang, and M. J. Rycroft, pp. 15–20, AIP.

Shao, X.-M., T. Hamlin, and D. M. Smith (2010), A closer examination of terrestrial gamma-ray flash-related lightning processes, *J. Geophys. Res.*, *115*, A00E30, doi:10.1029/2009JA014835.

Smith, D. M., M. Leventhal, R. Cavallo, N. Gehrels, J. Tueller, and G. Fishman (1996), All-sky search for transient sources near 0.5 MeV with the Burst and Transient Source Experiment (BATSE), *ApJ*, *471*, 783–795.

Smith, D. M., L. I. Lopez, R. P. Lin, and C. P. Barrington-Leigh (2005), Terrestrial gamma-ray flashes observed up to 20 MeV, *Science*, *307*, 1085–1088.

Smith, D. M., et al. (2006), The anomalous terrestrial gamma-ray flash of 17 january 2004, *Eos Trans. AGU*, *87*(52), AE31A1040.

Smith, D. M., J. Hazelton, W. Grefenstette, J. R. Dwyer, R. H. Holzworth, and E. H. Lay (2010), Terrestrial gamma ray flashes correlated to storm phase and tropopause height, *J. Geophys. Res.*, *115*, A00E49, doi:10.1029/2009JA014853.

Smith, D. M., et al. (2011a), A terrestrial gamma ray flash observed from an aircraft, *Geophys. Res. Lett.*, *116*, D20,124, doi:10.1029/2011JD016252.

Smith, D. M., et al. (2011b), The rarity of terrestrial gamma-ray flashes, *Geophys. Res. Lett.*, *38*, L08,807, doi:10.1029/2011GL046875.

Splitt, M. E., S. M. Lazarus, D. Barnes, J. R. Dwyer, H. K. Rassoul, D. M. Smith, B. Hazelton, and B. Grefenstette (2010), Thunderstorm characteristics associated with RHESSI identified terrestrial gamma ray flashes, *J. Geophys. Res.*, *115*, A00E38, doi:10.1029/2009JA014622.

Stanley, M. A., X.-M. Shao, D. M. Smith, L. I. Lopez, M. B. Pongratz, J. D. Harlin, M. Stock, and A. Regan (2006), A link between terrestrial gamma-ray flashes and intracloud lightning discharges, *Geophys. Res. Lett.*, *33*, L06,803, doi:10.1029/2005GL025537.

Tavani, M., et al. (2011), Terrestrial gamma-ray flashes as powerful particle accelerators, *Phys. Rev. Lett.*, *106*, 018,501, doi:10.1103/PhysRevLett.106.018501.

Ulmer, A. (1994), Gamma rays from grazing incidence cosmic rays in the earth's atmosphere, *ApJ*, *429*, L95–L97.

Virts, K. S., J. M. Wallace, M. L. Hutchins, and R. H. Holzworth (2012), A new ground-based, hourly global lightning climatology, *BAMS*, in press.

Williams, E., et al. (2006), Lightning flashes conducive to the production and escape of gamma radiation to space, *J. Geophys. Res.*, *111*, D16,209, doi:10.1029/2005JD006447.

Xiong, S., et al. (2012), Location prediction of electron TGFs, *J. Geophys. Res.*, *117*, A02,309, doi:10.1029/2011JA017085.

Table 1. The regions and dates in which the TTE data was collected

Regions	Dates	Julian Days	Exposure (hours)
Americas #1	16 July 2010 – 3 Nov 2010 plus 9 July, plus 11 July, less 28 & 29 Oct	2455393.5 – 2455504.5 plus 2455386.5 – 2455387.5, plus 2455388.5 – 2455389.5, less 2455497.5 – 2455499.5	208.0
Africa #1 – main	4 Nov 2010 – 26 Jan 2011	2455504.5 – 2455588.5	70.2
Africa #1 – North (control for TGFs)			35.8
Australia #1			27.5
Africa #2 – main	27 Jan 2011 – 30 March 2011	2455588.5 – 2455651.5	135.0
Africa #2 – North (control for TGFs)			26.8
Australia #2			87.4
Americas #2	31 March 2011 – 25 May 2011	2455651.5 – 2455707.5	120.5
Asia			44.5
Africa #3			72.8
Americas #2	26 May 2011 – 31 Aug 2011	2455707.5 – 2455805.5	191.8
Asia			71.9
Southeast Pacific (control)			69.3
Indian Ocean (control)			56.2
total continuous TTE, TGF-active			1029.6
total continuous TTE, control			188.1
total continuous TTE			1217.7
trigger time, TGF-active			7.1
total in TGF-active			1036.7
total			1224.8

Table 2. Search Results by Bin Width

Bin Width	Number TGFs Found	Median of Discovery Counts
25 μs	0	—
35 μs	2	28.5
50 μs	9	36.0
70.7 μs	32	46.0
100 μs	61	40.0
141 μs	109	54.0
200 μs	80	58.5
283 μs	66	56.0
400 μs	28	53.5
632 μs	24	65.5
1.0 ms	8	84.5
1.4 ms	2	67.0
2.0 ms	2	254.5
4.0 ms	1	748.0
8.0 ms	1	273.0
16.0 ms	0	—

Table 3. TGF / Lightning Ratio by region

Region	ratio
Americas	$(4.9 \pm 0.3) \times 10^{-4}$
Africa	$(2.3 \pm 0.2) \times 10^{-4}$
Asia	$(2.7 \pm 0.4) \times 10^{-4}$
Australia	$(8.6 \pm 1.0) \times 10^{-4}$
overall	$(3.8 \pm 0.2) \times 10^{-4}$

Table 4. TGF-active Regions – Sample Properties versus $P_{\rm joint}^{\rm corr}$

$P_{\rm joint}^{\rm corr}$ range	sample size	LAT-identified CRS fraction and (CRS number / data avail.)	WWLLN association rate and (number)
total search	598	0.26 (153/587)	0.24 (141)
$10^{-11} - 10^{-8}$	177	0.67 (116/173)	0.03 (5)
$10^{-14} - 10^{-11}$	56	0.36 (20/55)	0.27 (15)
$10^{-17} - 10^{-14}$	28	0.32 (9/28)	0.18 (5)
$10^{-20} - 10^{-17}$	33	0.06 (2/33)	0.30 (10)
$< 10^{-20}$	304	0.02 (6/298)	0.35 (106)
$\leq 10^{-11}$	421	0.09 (37/414)	0.32 (136)
$\leq 10^{-11}$ – CRS	384	0 (0/377)	0.35 (133)
$\leq 10^{-11}$ – CRS + trigger	425	0 (0/417)	0.33 (142)

Table 5. Control Regions – Sample Properties versus $P_{\rm joint}^{\rm corr}$

$P_{\rm joint}^{\rm corr}$ range	sample size	LAT-identified CRS fraction and (number)	WWLLLN association rate
total search	34	0.85 (29)	0
$10^{-11} - 10^{-8}$	29	0.86 (25)	0
$10^{-14} - 10^{-11}$	3	1.00 (3)	0
$10^{-17} - 10^{-14}$	2	0.50 (1)	0
$10^{-20} - 10^{-17}$	0	0 (0)	0
$< 10^{-20}$	0	0 (0)	0
$\leq 10^{-11}$	5	0.80 (4)	0
$\leq 10^{-11}$ – CRS	1	0 (0)	0
$\leq 10^{-11}$ – CRS + trigger	1	0 (0)	0

Figure 1. The green polygon shows the first region for the Americas, used from 9 July 2010 to 3 November 2010 to collect continuous TTE data. The orange cross-hatched region denotes the South Atlantic Anomaly (SAA), a region of high trapped particle fluxes. Inside the SAA the GBM detectors are turned off to preserve their lifetime. The blue lines show the tracks of the orbit of Fermi on 1 August 2010. When Fermi enters the one of the TTE regions and the detectors are on (i.e., Fermi is outside of the SAA), continuous TTE data are collected (bold blue lines). On 1 August 2010 Fermi entered the first Americas region nine times, providing 1.93 hours of continuous TTE.

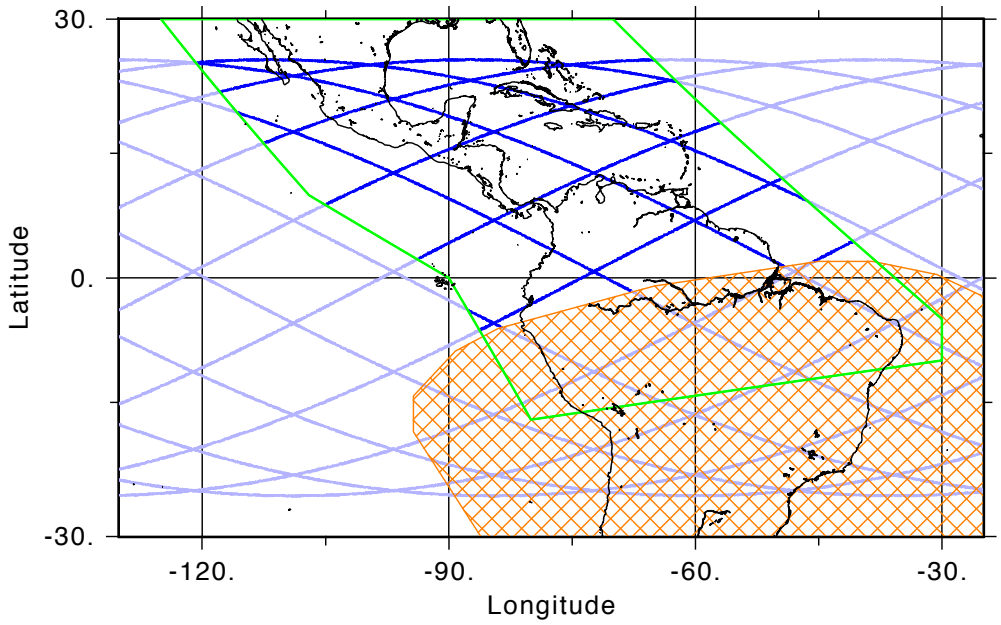

Figure 2. The green polygons show the boundaries of the ten regions that were used to collect the continuous TTE data analyzed in this paper. The ten regions were not in place simultaneously; their time intervals are listed in Table 1. The orange cross-hatched region denotes the SAA. The dotted lines at ±25.6° latitude show the inclination of the orbit of Fermi. The grey scale depicts the exposure time of the continuous TTE, totaling 1217.7 hours, accumulated into approximately 1° square pixels (the pixel dimensions are slightly adjusted to maintain equal areas). There is increased exposure at higher latitudes due to the orbit. The cyan circles show the 385 candidates found by the offline search of the continuous TTE according to the seven requirements (section 2.2): 384 in the TGF-active regions and 1 in the control regions (Southeast Pacific, Indian Ocean, and northern Africa).

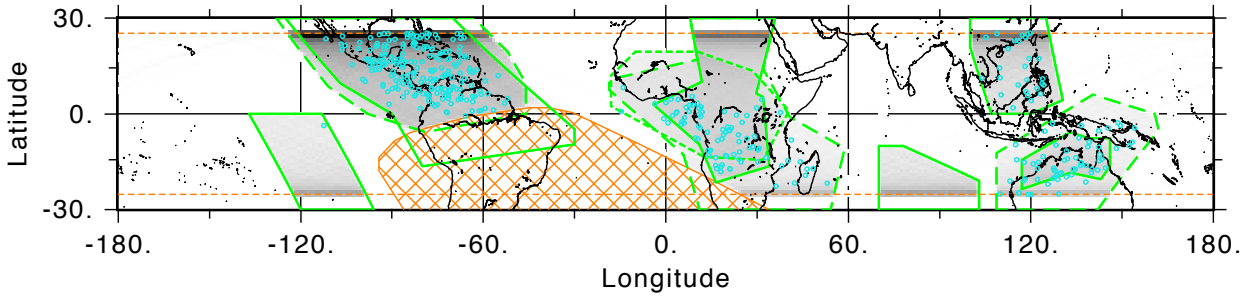

Figure 3. Time histories in the GBM detectors for an example TGF found by the offline search in the continuous TTE. Time histories are shown for BGO 0, BGO 1 and the sum of the twelve NaIs. The thin horizontal lines show the expected background levels, defined by averaging 10 seconds of data. These levels are 0.173, 0.221 and 1.182 counts per bin for the BGO 0, BGO 1 and NaI detectors, respectively. The TGF is found at highest significance on the 141 μs binning in the bin starting at 21:42:09.660116 UT on 16 August 2011. Times on the figure are relative to this time and the histograms at binned using this resolution. The counts in the discovery bin are 4 for BGO 0, 7 for BGO 1 and 16 for the sum of the NaIs, giving cumulative Poisson probabilities of 3.25×10^{-5}, 4.27×10^{-9} and 2.29×10^{-13}, respectively. Allowing for $N_{\rm bins} = 7879433$ of these 141 μs bins in the datafile, $P_{\rm joint}^{\rm corr} = 2.5 \times 10^{-19}$ (eq. 2). If there were only one detector, perhaps the event would not be significant, but with simultaneous, independent detections in three different "detectors" the signal is highly significant.

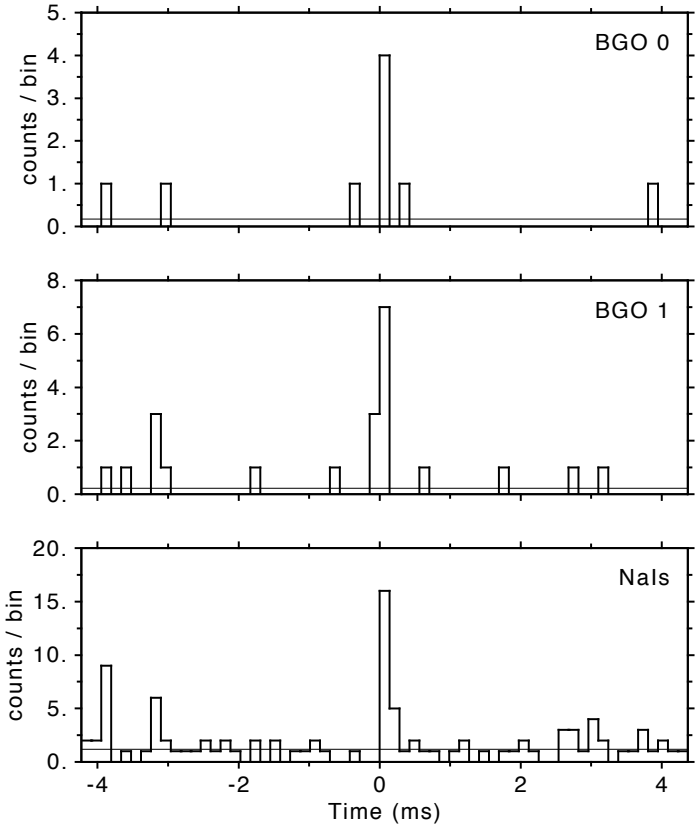

Figure 4. Search parameters for the 425 TGFs and TEBs of the reliable sample. Results for the 384 TGFs found with the offline search applied to the continuous TTE are shown in cyan. The offline-search "rediscovered" all 41 triggered events (39 TGFs and 2 TEBs) – their search parameters are shown in red. TGFs are shown with open symbols and the two TEBs with filled symbols. Three parameters are shown: 1) The corrected, joint Poisson probability $P_{\rm joint}^{\rm corr}$ (equation 2), 2) discovery bin width, which is the width of the search bin that produces the most significant (smallest) value of $P_{\rm joint}^{\rm corr}$, and 3) discovery counts, the total number of counts in this bin. On some of the sub-figures a very small number of events have off-scale values – these are depicted with arrows. Three events have off-scale values of $P_{\rm joint}^{\rm corr}$, below 10^{-300}. One TEB has a large, off-scale number of discovery counts, 748. Discovery bin width values < 1 ms for triggered TGFs are shifted 5% for clarity in panels A & B. Due to the overlapping trials and multiple requirements, the $P_{\rm joint}^{\rm corr}$ values should not be strictly interpreted as probabilities that excesses are statistical fluctuations. A) Discovery counts versus discovery bin width, B) $P_{\rm joint}^{\rm corr}$ versus discovery bin width, C) $P_{\rm joint}^{\rm corr}$ versus discovery counts, D) Histogram of the numbers of TGFs and TEBs found versus discovery counts, E) Histogram of the numbers of TGFs and TEBs found versus discovery bin width.

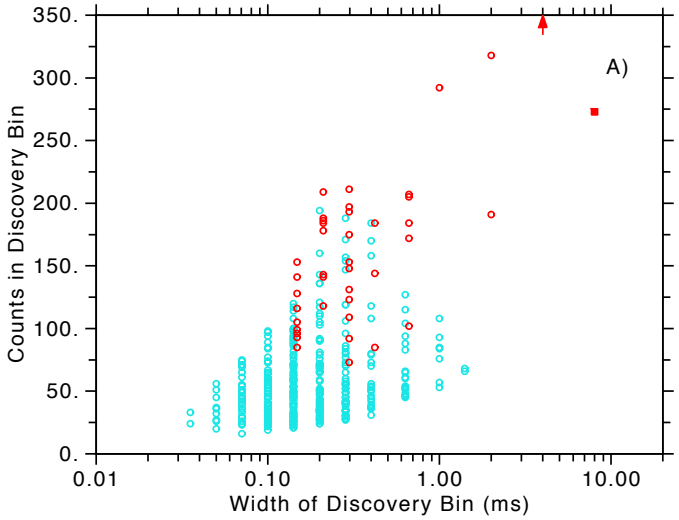

Figure 4. Continued: panels B, C & D.

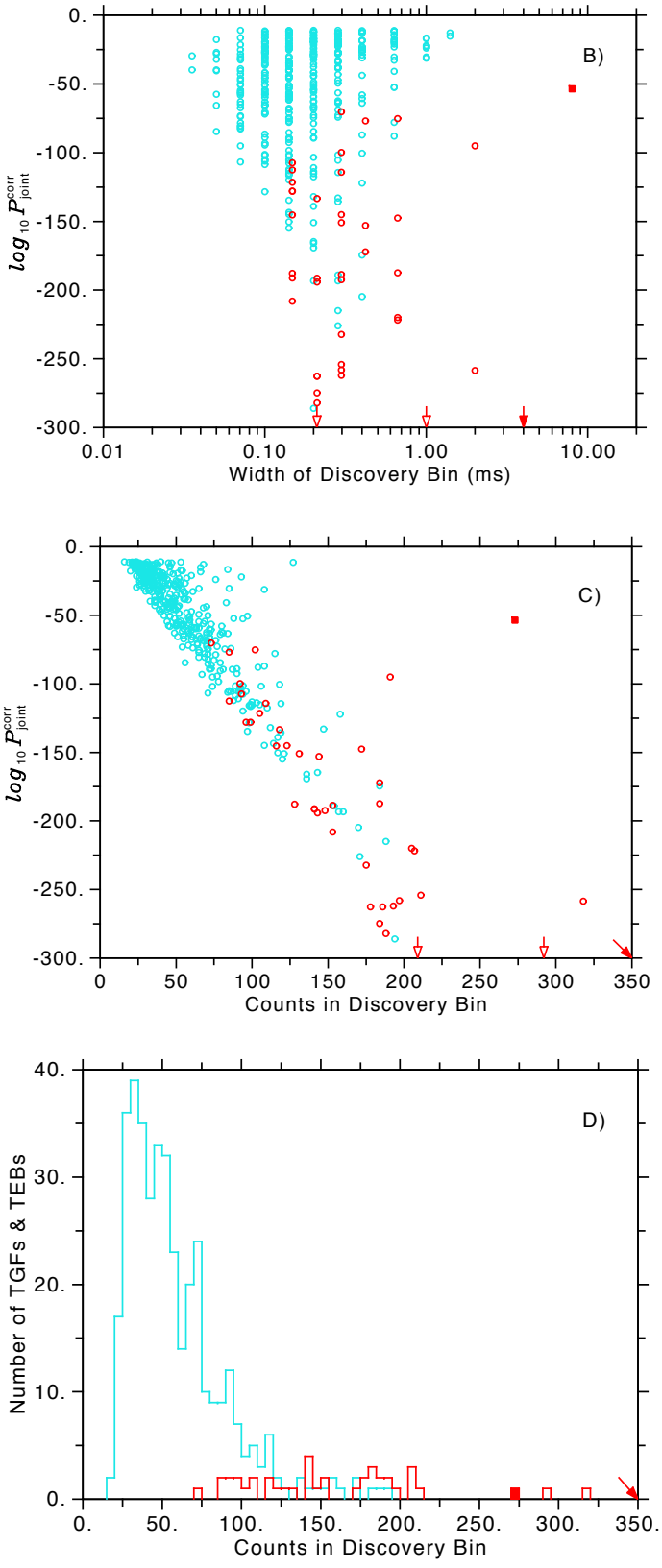

Figure 4. Continued: panel E.

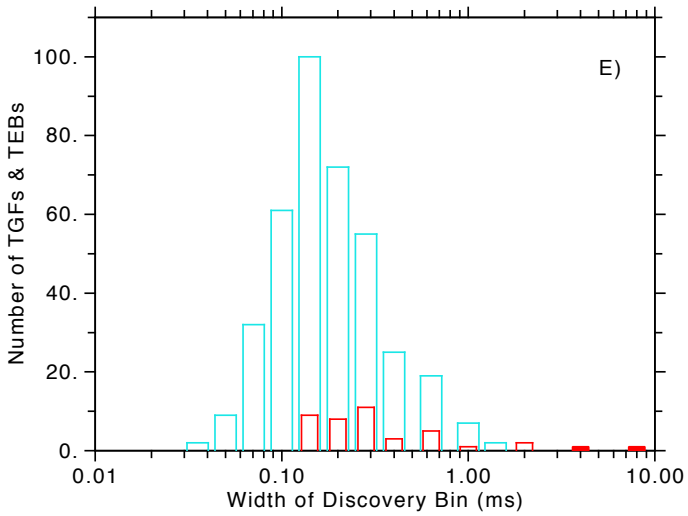

Figure 5. Locations of Fermi for the reliable sample of 425 TGFs/TEBs. The 384 TGFs found by the offline search of the continuous TTE are shown in cyan while the 41 triggered TGFs/TEBs are shown in red. TGFs are depicted with open circles and TEBs with filled squares. There are (a) 227 TGFs and 1 TEB in the Americas (including 18 triggered), (b) 90 TGFs in Africa (including 6 triggered), and (c) 106 TGFs and 1 TEB in Asia and Australia (including 17 triggered).

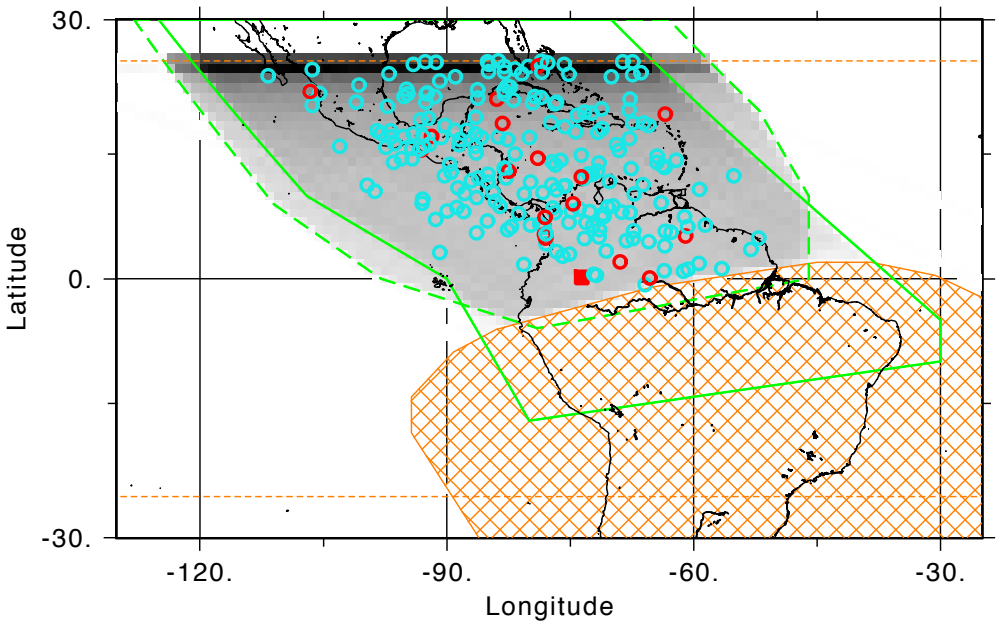

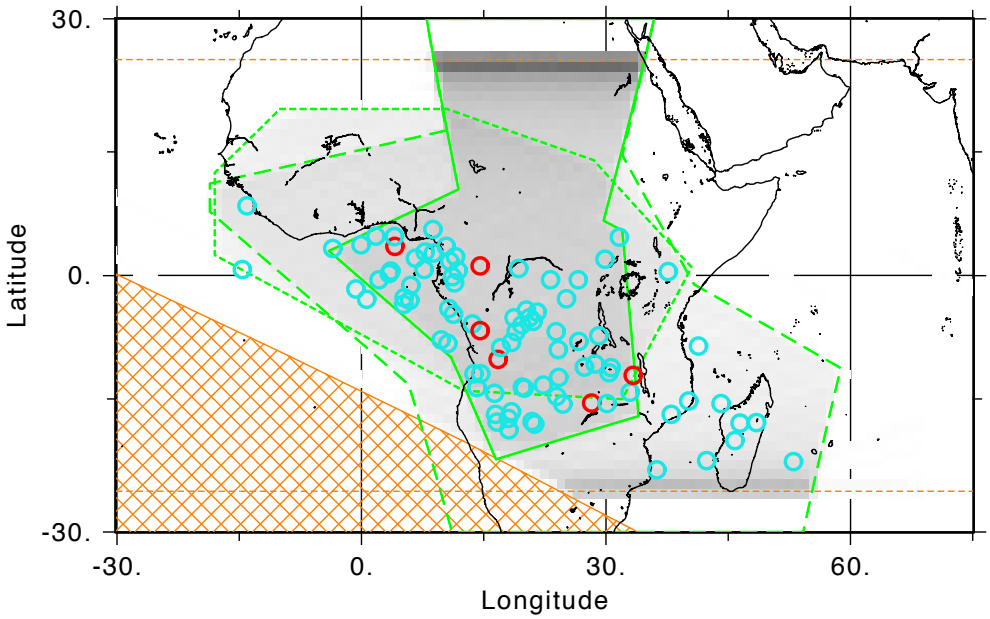

Figure 5. Continued: panel C.

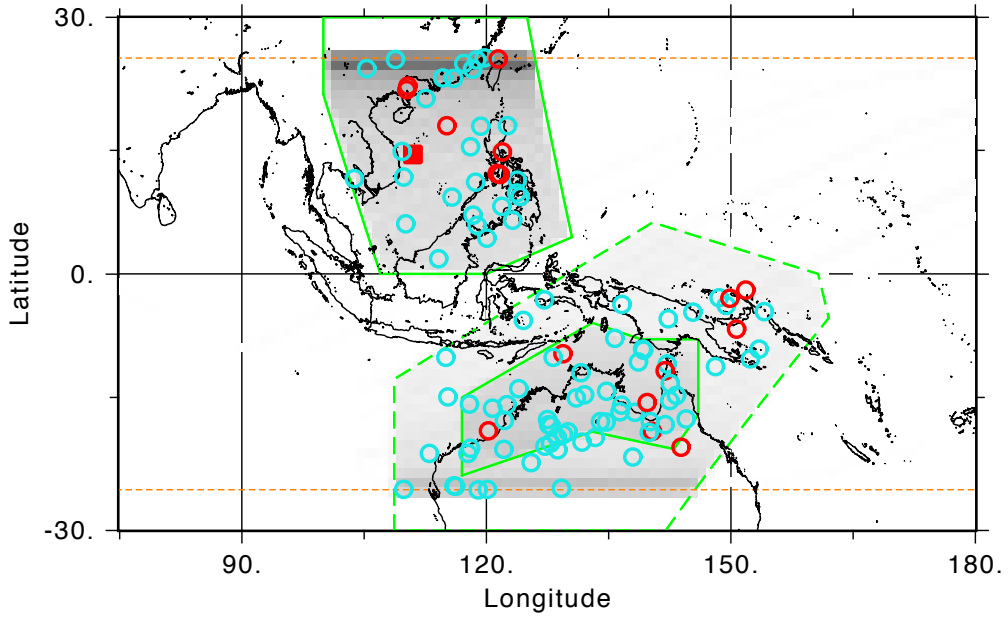

Figure 6. The locations measured by WWLLN for the events with associated WWLLN locations: 141 TGFs (open circles) and one TEB (filled square). This includes 133 continuous TTE TGFs (cyan) and 9 of the triggered TGFs/TEBs (red). There are (a) 89 TGFs in Americas, (b) 26 TGFs in Africa, and (c) 26 TGFs and 1 TEB in Asia and Australia. Association rates by region are (a) 39% , (b) 29%, and (c) 25%.

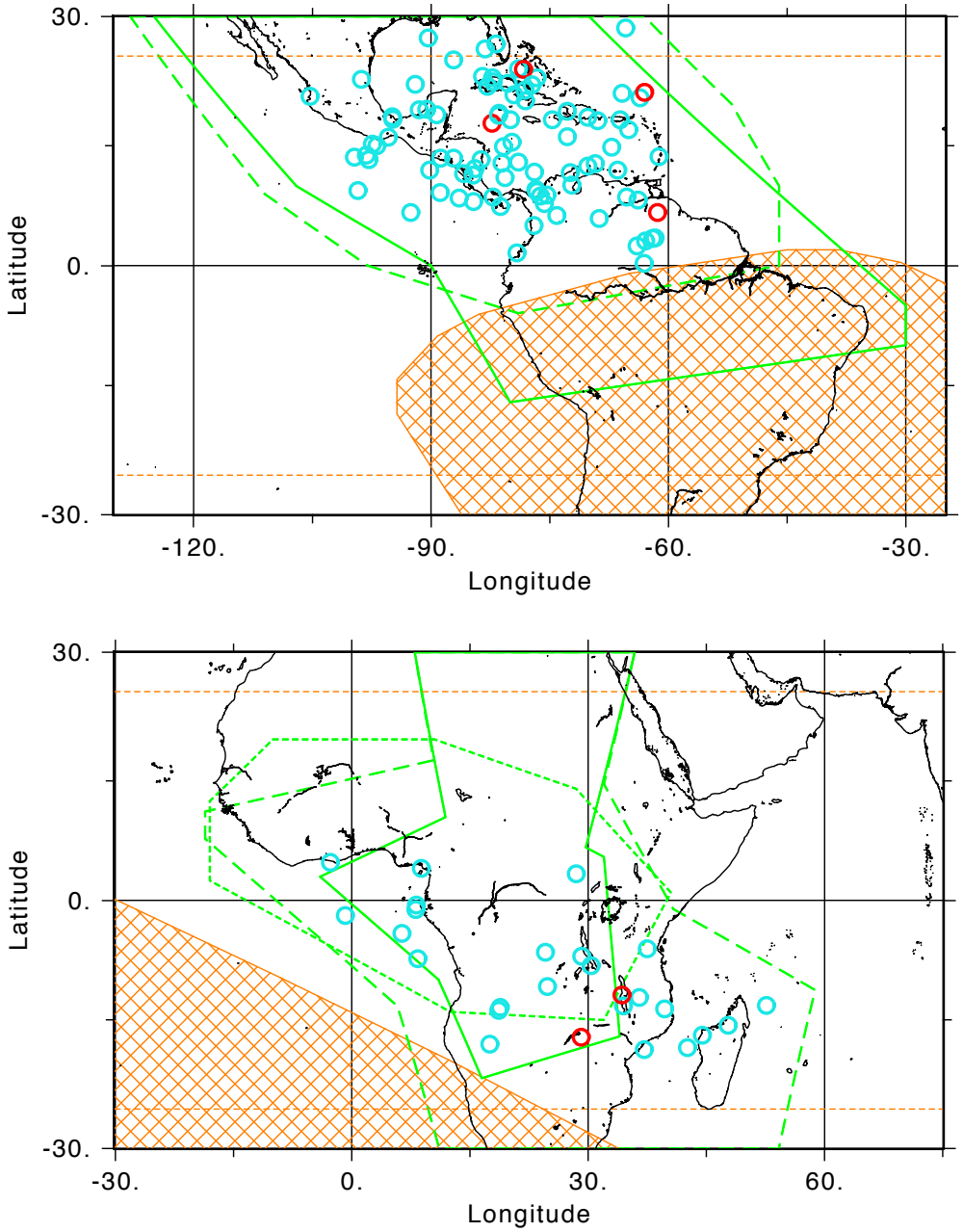

Figure 6. Continued: panel C.

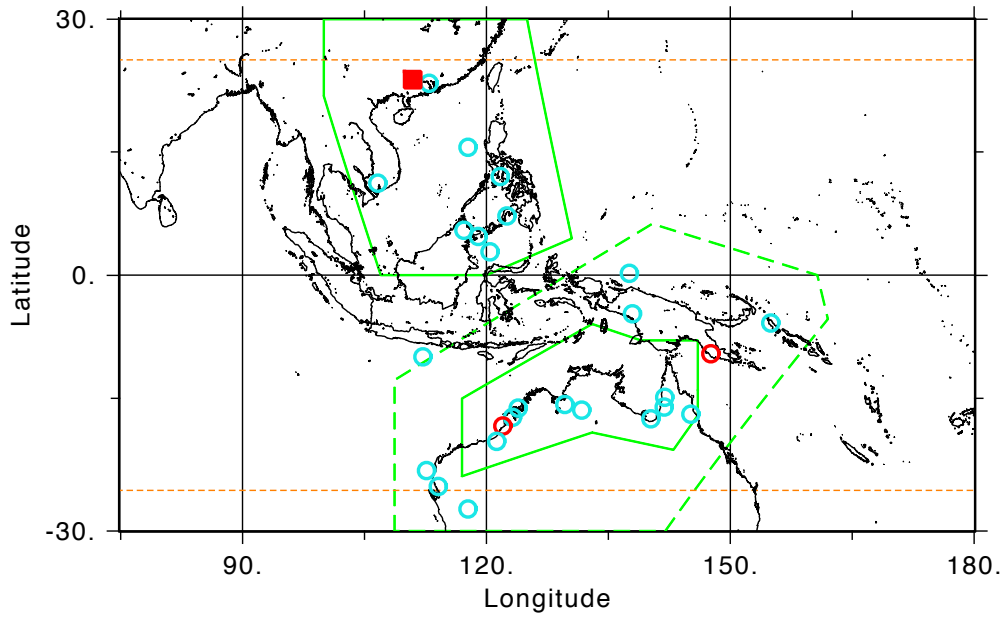

Figure 7. The differences between the nadirs of Fermi and the WWLLN-determined locations for 141 TGFs. The TEB is omitted because its separation has a different meaning. The circles denote the WWLLN locations, with cyan for continuous TTE TGFs and red for triggered TGFs. The black lines run between the nadirs of the spacecraft at the time of the TGFs and the WWLLN locations.

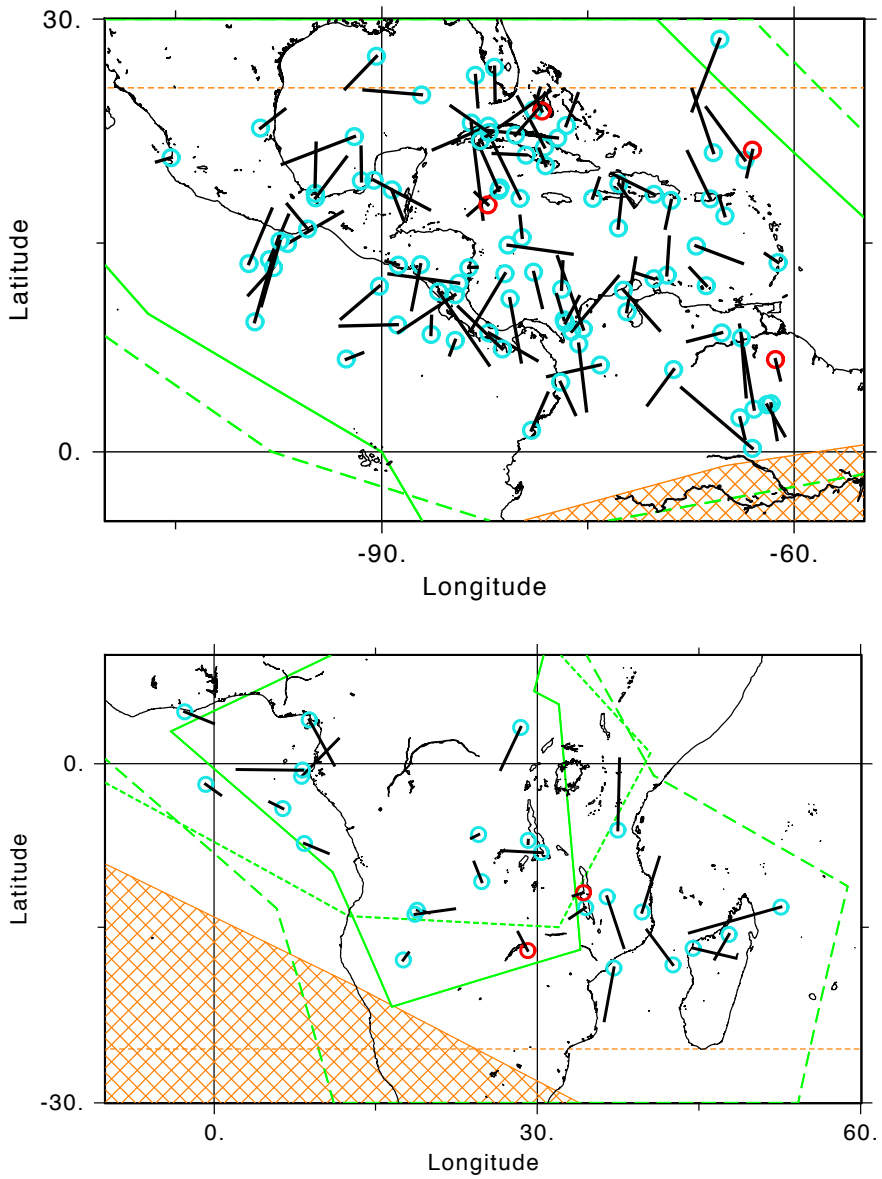

Figure 7. Continued: panel C.

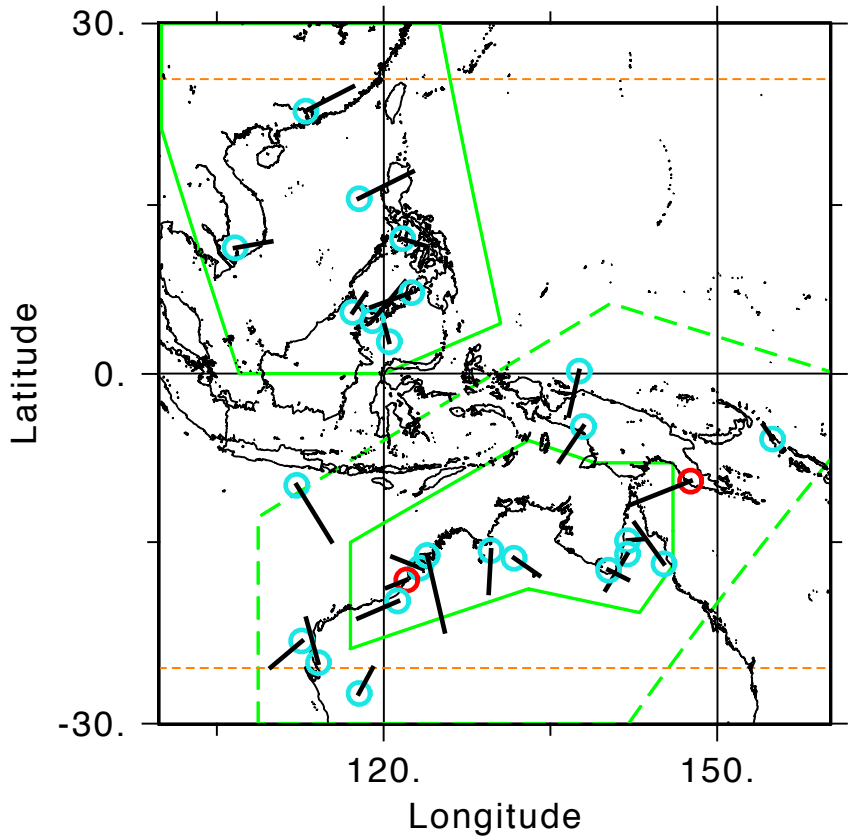

Figure 8. TGF properties versus the offsets between the nadirs of Fermi for the TGFs and the source locations, as determined with WWLLN. Sub-figures A and B show histograms. The black histograms show 141 TGFs with WWLLN associations, including both offline search TGFs and triggered TGFs. All figures omit the TEB with a WWLLN association because its nadir-source separation has a different meaning. A) Histograms of the observed numbers of TGFs. Red histogram: A subset of the black histogram, the 8 triggered TGFs. Green histogram: the area observed as a function of offset for a spherical earth [*Gjesteland et al.*, 2011]; arbitrary normalization. B) The GBM TGF rate density versus offset. The rate is for the total observation time of 1036.7 hours and is converted to the GBM TGF rate density by dividing the GBM / WWLLN nadir-source offset measurements by the GBM / WWLLN association rate of 0.334. The orange curve shows an empirical model: a uniform density is assumed to 300 km, then the density decreases with increasing offset. C) Scatter plot of the counts in the discovery bin versus the offset. The eight triggered TGFs are shown with red symbols and the 133 TGFs found only with the offline search with cyan symbols.

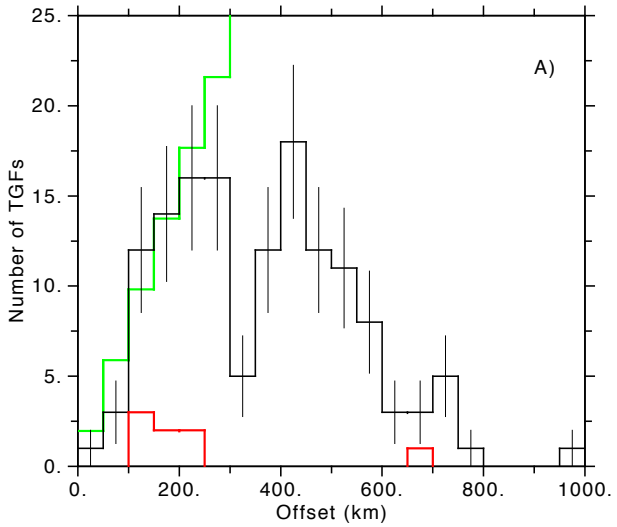

Figure 8. Continued: panel B & C.

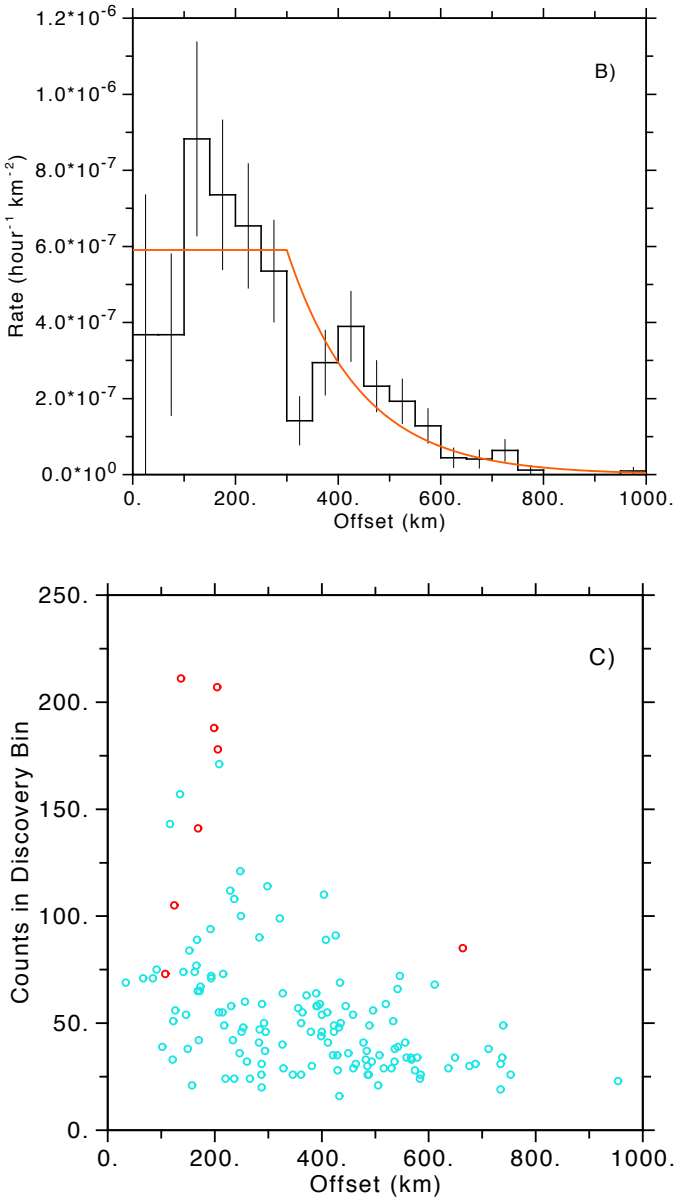

Figure 9. Histograms of the diurnal distribution of TGFs binned by local solar time. Black: the total sample of 423 TGFs, triggered and continuous TTE. Dashed cyan: the 384 TGFs found by the offline search in the continuous TTE.

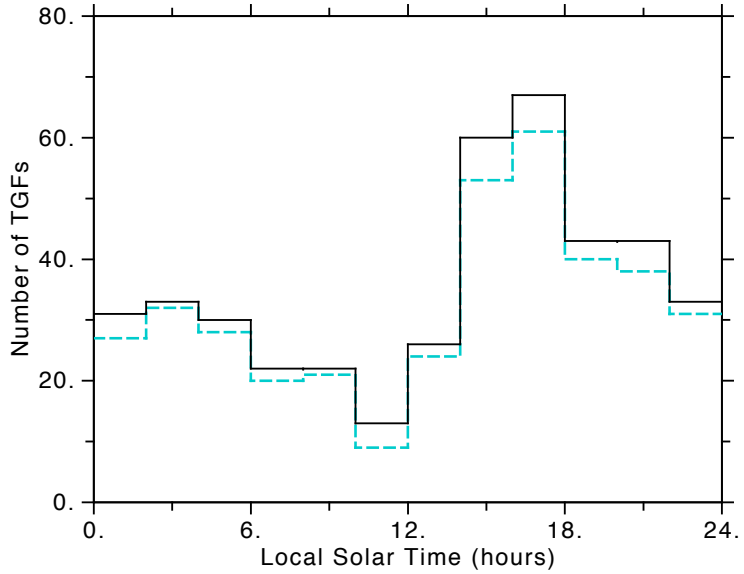

Figure 10. A) Histogram of t_{90} values for 425 pulses from 423 TGFs. Black: all of the TGFs in the sample, both offline search of continuous TTE and triggered TGFs. Dashed cyan: A subset of the black histogram: 386 pulses from 384 TGFs found by the offline search in the continuous TTE. Red: A subset of the black histogram: 39 pulses from 39 triggered TGFs. B) Same as for A except for t_{50}. C) Counts within the t_{90} interval.

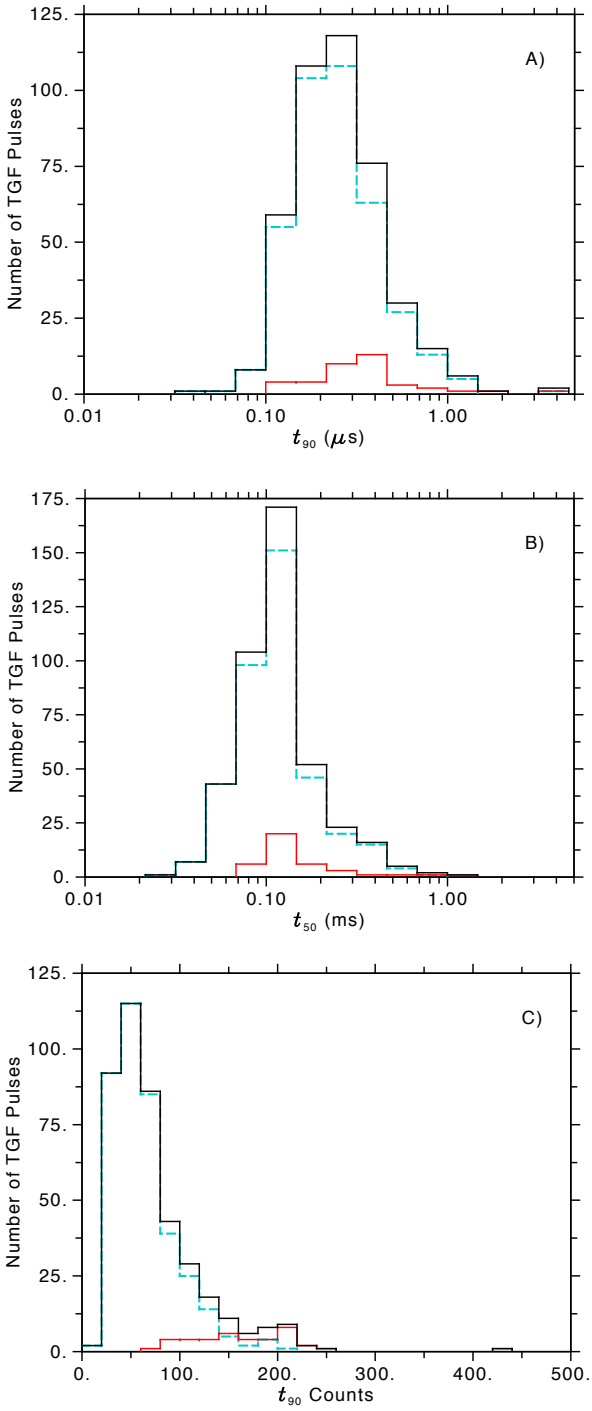

Figure 11. The distributions of the deadtime fraction in the BGO detectors for two groups of TGFs. The deadtime fraction is for the BGO detector with the highest deadtime fraction and is calculated as the fraction of the time that the detector is unable to detect a count during the discovery bin (equation 3). The blue histogram is for the 109 TGFs that are most significant in the offline search on the 141 μs bin width. The orange histogram is for the shortest TGFs found with the offline search, two on the 35 μ bin width and nine on the 50 μs bin width. For comparison purposes the distributions are normalized.

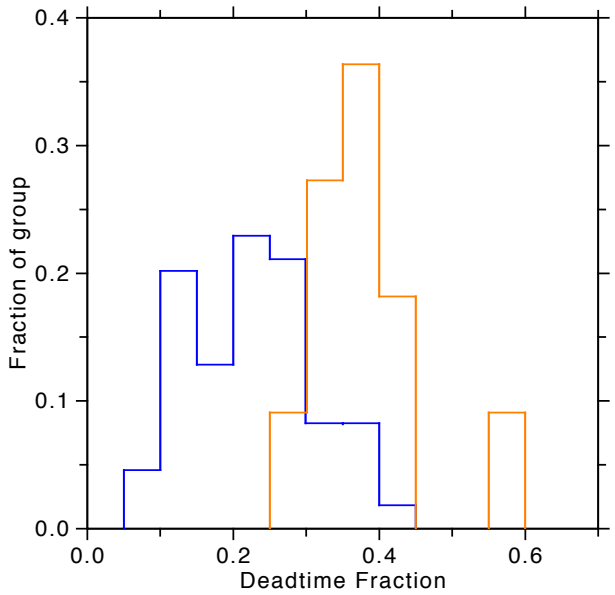

Figure 12. Comparisons of duration measures and results. Cyan points are TGFs found in the offline search of the continuous TTE and red points are triggered TGFs. A) t_{90} compared to t_{50} for 425 pulses from 423 TGFs, B) Discovery bin width compared to t_{90} for the 421 TGFs with single values of t_{90} (discovery bin width values < 1 ms for triggered TGFs are shifted 5% for clarity), C) Comparison of the counts in the discovery bins to the counts in the t_{90} intervals for the 421 TGFs. One very strong TGF with 431 counts in the t_{90} interval and 318 counts in the discovery bin is off-scale (arrow).

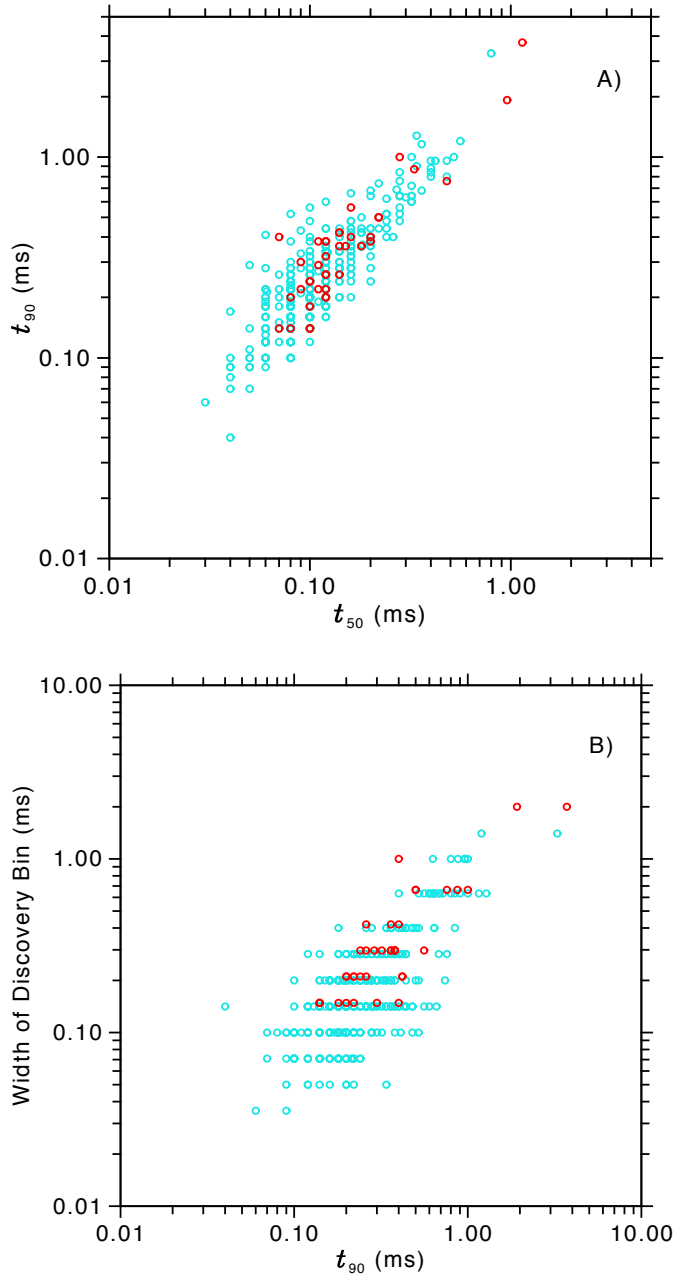

Figure 12. Continued: panel C.

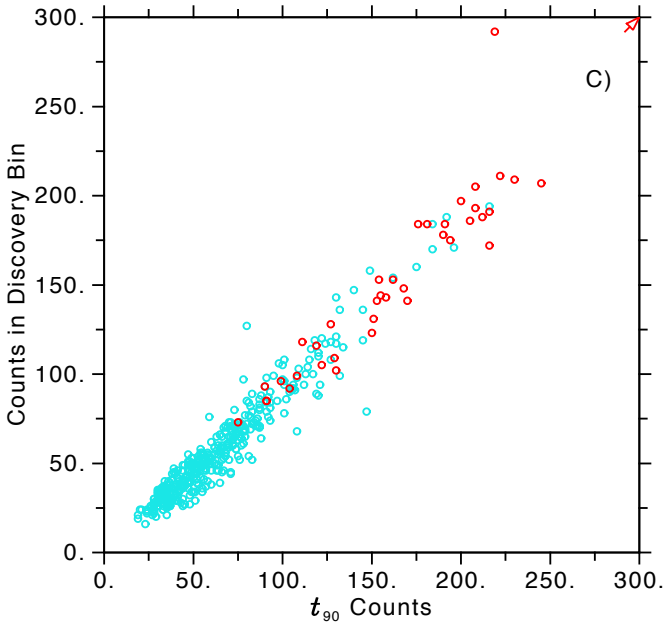

Figure 13. TGFs found by applying the offline search to 86.95 hours of TTE data acquired from 952 GRB triggers. The grey scale shows the exposure, the green circles show the five or six TGFs. The event in the Indian Ocean is probably a cosmic ray; the nature of the event in Egypt is uncertain. The orange cross-hatched region denotes the SAA.

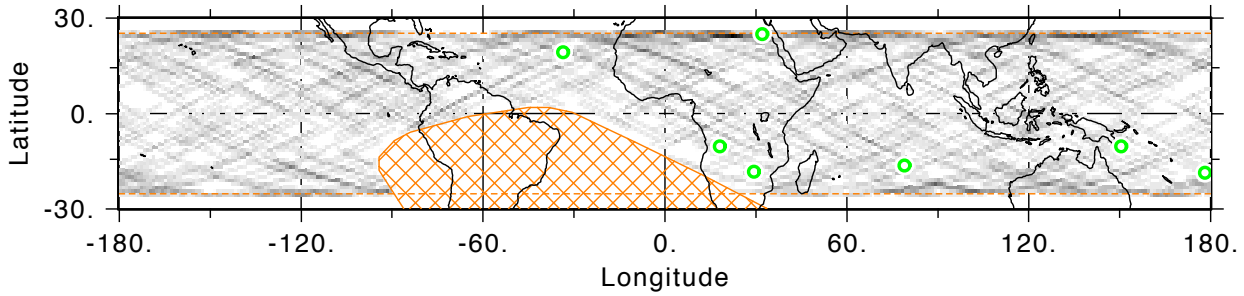

Figure 14. Map of WWLLN lightning locations (green squares) detected within 600 s of a TGF found in the TTE data of a GRB. The location of Fermi is shown with a red "X", about which is drawn a circle of 300 km radius. While the closest land, the Cape Verde Islands (lower right of map), is more then 900 km from the nadir of Fermi, an active storm is much closer, as shown by the cluster of WWLLN lightning locations.

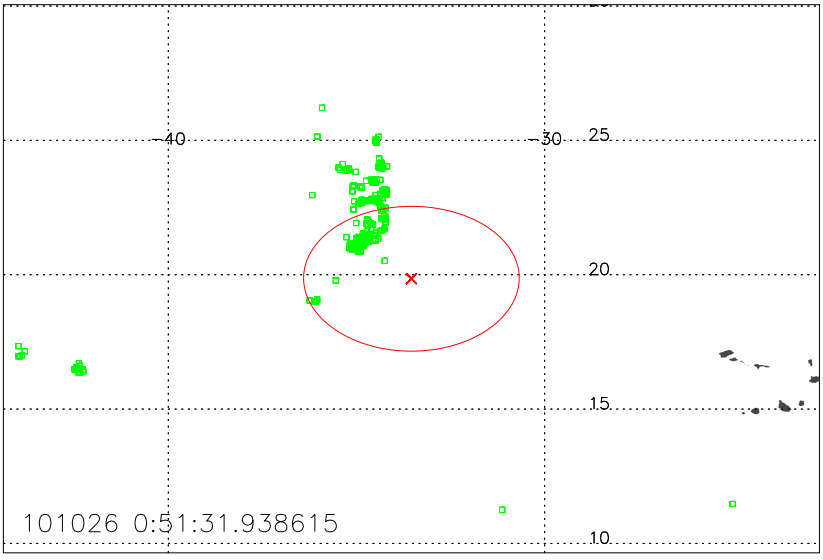

Figure 15. The magenta circles show the 632 candidates found in the initial offline search using the relaxed threshold of $P_{\rm joint}^{\rm corr} = 10^{-8}$ and before cosmic ray showers were removed using LAT calorimeter data: 598 in the TGF-active regions and 34 in the control regions (Southeast Pacific, Indian Ocean, and northern Africa). Tightening the $P_{\rm joint}^{\rm corr}$ threshold to 10^{-11} and using the LAT calorimeter data to remove cosmic rays removed 214 candidates from the TGF-active regions and all but one from the control regions (Tables 4 & 5), creating the reliable TGF sample shown in Figure 2.